

Material Matters™

Volume 9, Number 2

ALDRICH
Materials Science



Inorganic Materials in Biomedical Applications

Nanotechnology Meets Biotechnology

BIOMEDICAL IMPLANT DEVICES

FABRICATED FROM LOW YOUNG'S MODULUS TITANIUM ALLOYS DEMONSTRATING HIGH MECHANICAL BIOCOMPATIBILITY

BIO-INSPIRED "GREEN" SYNTHESIS

OF NANOMATERIALS AND THEIR APPLICATIONS

NANOFUIDS FOR BIOMEDICAL APPLICATIONS

USING SPHERICAL IRON OXIDE MAGNETIC NANOPARTICLES
FABRICATED BY HIGH-POWER PHYSICAL EVAPORATION

SILVER NANOMATERIALS

FOR BIOLOGICAL APPLICATIONS

SIGMA-ALDRICH®

Introduction

Welcome to the second issue of *Material Matters*™ for 2014. Our focus this issue is the intersection of inorganic materials and biological systems. From alloys to nanoparticles, inorganic materials play a crucial role in modern medicine. This includes applications such as implants, drug delivery and imaging, all of which take advantage of the unique properties of inorganic materials to enhance patient outcomes. These technologies require low-cost and environmentally sustainable synthesis and production routes. Meeting these challenges forms the basis of an exciting field of study poised to enhance the quality of life.

In our first article, Professor Misuo Niinomi (Institute for Materials Research, Tohoku University, Japan) discusses the properties and applications of alloys used in biomedical implants. Because of their strength and reliability, biomedical alloys have become essential components of joint replacements, bone screws and dental materials. Titanium-based alloys promise significant improvements over traditional alloys, including better biocompatibility and mechanical properties that more closely match those of bone. In this article, Professor Niinomi discusses recent efforts to optimize the properties of these new alloys in order to improve biomedical implants.

Professor Siddharth Patwardhan (University of Strathclyde, Scotland) in our second article describes a biologically-inspired synthetic route to produce silica nanomaterials. Silica nanomaterials are proven to be nontoxic and can be used in applications including drug delivery, cosmetics and chromatography. Although many methods for template-directed synthesis of silica nanomaterials already exist, most rely on energy intensive reaction conditions and the use of toxic precursors. In contrast, this article describes a green synthesis route for bio-inspired silicas with tunable properties as well as their applications.

In the third article, Professor G. V. Kurlyandskaya (Ural Federation University, Russia, and University of Basque Country, Spain) reviews two new synthesis methods for magnetic nanoparticles used in biomedical research. While these materials are of great interest, concerns regarding batch-to-batch reproducibility and scalability have previously limited their implementation. To this end, the authors describe two methods of synthesis—Electric Explosion of Wire and Laser Target Evaporation—and the results of their synthesis and characterization.

Finally, Dr. Steven Oldenburg (nanoComposix, Inc., USA) presents an overview of current applications of silver nanoparticles. The antibacterial and optical properties of nanoscale silver allow for wide utility, but precisely engineered particles are necessary to fully realize these benefits. This article highlights the effects of particle size and morphology on the optical properties and showcases potential applications for imaging and nanomedicine.

Each article in this publication is accompanied by a list of relevant materials available from Aldrich® Materials Science. For additional product information, visit us at aldrich.com/matsci. Lastly, “please bother us” with your comments and suggestions for *Material Matters*, as well as your product suggestions at matsci@sial.com. We look forward to hearing from you.

About Our Cover

The areas of nanotechnology and biotechnology continue to blend closer together in a rapidly changing academic and commercial environment. The cover art illustrates the convergence of these two technologies through the development of stronger, more biocompatible implants. It also represents the use of nanomaterials for a variety of biomedical applications such as magnetic iron nanoparticles to create nanofluids that demonstrate high biocompatibility; silver nanoparticles with their unique antimicrobial and optical properties and their potential uses in drug delivery, bioimaging, targeting, and tagging. Aldrich® Materials Science is proud to help enable the advancements in these technologies with a large variety of innovative materials.



Adam Raw, Ph.D.
Aldrich Materials Science

Material Matters™

Vol. 9, No. 2

Aldrich Materials Science
Sigma-Aldrich Co. LLC
6000 N. Teutonia Ave.
Milwaukee, WI 53209, USA

To Place Orders

Telephone 800-325-3010 (USA)
FAX 800-325-5052 (USA)

International customers, contact your local Sigma-Aldrich office (sigma-aldrich.com/worldwide-offices).

Customer & Technical Services

Customer Inquiries 800-325-3010
Technical Service 800-325-5832
SAFC® 800-244-1173
Custom Synthesis 800-244-1173
Flavors & Fragrances 800-227-4563
International 314-771-5765
24-Hour Emergency 314-776-6555
Safety Information sigma-aldrich.com/safetycenter
Website sigma-aldrich.com
Email aldrich@sial.com

Subscriptions

Request your **FREE** subscription to *Material Matters*:

Phone 800-325-3010 (USA)
Mail Attn: Marketing Communications
Aldrich Chemical Co., Inc
Sigma-Aldrich Co. LLC
P.O. Box 2060
Milwaukee, WI 53201-2060
Website aldrich.com/mm
Email sams-usa@sial.com

Material Matters (ISSN 1933-9631) is a publication of Aldrich Chemical Co., Inc. Aldrich is a member of the Sigma-Aldrich Group.

Online Versions



Explore previous editions of *Material Matters*. Visit aldrich.com/materialmatters



Now available for your iPad®
aldrich.com/mm

©2014 Sigma-Aldrich Co. LLC. All rights reserved. SIGMA, SAFC, SIGMA-ALDRICH, ALDRICH, SUPELCO, and SAFC Hitech are trademarks of Sigma-Aldrich Co. LLC, registered in the US and other countries. FLUKA is a trademark of Sigma-Aldrich GmbH. Material Matters is a trademark of Sigma-Aldrich Co. LLC. iPad is a registered trademark of Apple Inc. Celite is a registered trademark of Imerys Minerals California, Inc. Sigma brand products are sold through Sigma-Aldrich, Inc. Purchaser must determine the suitability of the product(s) for their particular use. Additional terms and conditions may apply. Please see product information on the Sigma-Aldrich website at www.sigmaaldrich.com and/or on the reverse side of the invoice or packing slip.

Table of Contents

Articles

Biomedical Implant Devices Fabricated from Low Young's Modulus Titanium Alloys Demonstrating High Mechanical Biocompatibility	39
Bio-inspired "Green" Synthesis of Nanomaterials and Their Applications	52
Nanofluids for Biomedical Applications Using Spherical Iron Oxide Magnetic Nanoparticles Fabricated by High-Power Physical Evaporation	58
Silver Nanomaterials for Biological Applications	64

Featured Products

Precursors for Biomedical alloys A selection of high-purity metal precursors for biomedical alloys	47
Mesoporous Silicas A list of silicas and functionalized silicas for biomaterials synthesis	55
Mesoporous Materials Aluminum- and carbon-based mesoporous materials	55
Silicon Nanomaterials A selection of silicon-based nanopowders and dispersions	55
Silica Solution Deposition Precursors A list of silicon-based solution deposition precursors	56
Iron Nanoparticles A selection of iron nanopowders and dispersions	62
Magnetic Nanoparticles A list of other inorganic magnetic nanopowders and dispersions	62
Iron Wires High-purity iron wires for use in magnetic nanoparticle synthesis	66
Silver Nanomaterials Silver nanopowders, nanowires and dispersions for biological applications	67
Silver Salts A selection of silver salt precursors for the synthesis of silver nanomaterials	68
Gold Nanorods A selection of gold nanorods with a large range of optical properties	68

Your Materials Matter



Bryce P. Nelson, Ph.D.
Aldrich Materials Science Initiative Lead

We welcome fresh product ideas. Do you have a material or compound you wish to see featured in the Aldrich® Materials Science line? If it is needed to accelerate your research, it matters. Send your suggestion to matsci@sial.com for consideration.

Professor Shanlin Pan at the University of Alabama, USA, inspired the addition to our catalog of reactant-free, monodisperse 15 nm gold nanoparticles stabilized in 0.1 mM PBS (**Aldrich Prod. No. 777099**). These gold nanoparticles make ideal plasmonic materials in applications that require high sensitivity and a minimum amount of contaminants. This product is particularly suited for the passive adsorption of proteins and other ligands as well as for use in surface enhanced Raman labeling,¹ sensing and detection,² biological targeting,³ plasmonics,⁴ and electronics,⁵ among many other applications.

References

- (1) Furusho, H.; Oishi, M.; Kishi, T.; Yasumori, A.; Nagasaki, Y., *Chem. Lett.* **2010**, 39, 52.
- (2) Lian, W.; Liu, S.; Yu, J.; Li, J.; Cui, M.; Xu, W.; Huang, J., *Biosensors & Bioelectronics* **2013**, 44, 70-76.
- (3) Kang B.; Mackey, M.A.; El-Sayed, M.A., *J Am Chem Soc.* **2010**, 132(5), 1517-9.
- (4) Liang C.C.; Liao, M.Y.; Chen, W.Y.; Cheng, T.C.; Chang, W.H.; Lin, C.H., *Opt Express.* **2011**, 19(5), 4768-76.
- (5) Park, I.; Ko, S.H.; Pan, H.; Grigoropoulos, C.P.; Pisano, A.P.; et al., *Adv. Mater.* **2008**, 20, 489.

Gold Nanoparticles

Au	Au
FW 196.97	MW 196.97
Particle size diameter 15 nm
Concentration OD 1
Stabilizer 0.1 mM PBS, reactant free
777099-25ML	25 mL
777099-100ML	100 mL

ELEMENTAL BUILDING BLOCKS

Pure Elements from Goodfellow Now Available

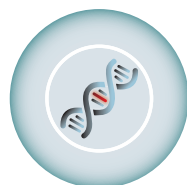
High-purity metals play an essential role in applications such as biomedical alloys and physical vapor deposition. Advances in materials science require precursors that ensure optimum properties, performance, and quality and Aldrich® Materials Science is proud to offer our customers over 9,900 elemental materials from Goodfellow Cambridge Ltd., a leading international supplier of metals and materials for research and industry.

This enhanced selection is ideal for research laboratories seeking precision materials for advanced technologies. As materials innovation requires not only the correct composition but also form, we are excited to announce the enhancement of our selection of materials including:

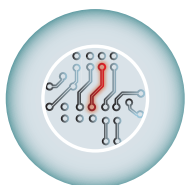
- Foils
- Rods
- Wires
- Tubes
- Fibers
- Bars
- Sheets
- Foams
- Honeycombs
- Spheres
- Powders
- Meshes

For a full selection of ultra-high purity materials, visit go.sigmaaldrich.com/itselemental

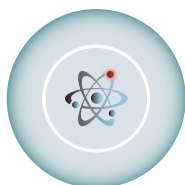
Goodfellow



BIOMEDICAL



ELECTRONICS



ENERGY

Representative Materials

Name	Dimensions	Specifications	Prod No.
Silver, Foil	0.1 mm thickness	Trace metal purity 99.95+%	GF23006797
Carbon, Fiber	0.007 mm diameter	Tex number 200, 3,000 filaments	GF20790558
Platinum, Rod	200 mm × 1.25 mm	Trace metal purity 99.95%	GF44306625
Tantalum, Tube	OD 0.31 mm, ID 0.19 mm	Trace metal purity 99.9%	GF33615716
Niobium, Insulated Wire	0.125 mm diameter	insulated wire, polyimide insulation	GF76912308

BIOMEDICAL IMPLANT DEVICES

FABRICATED FROM LOW YOUNG'S MODULUS TITANIUM ALLOYS

DEMONSTRATING HIGH MECHANICAL BIOCOMPATIBILITY



Mitsuo Niinomi, Masasaki Nakai*
 Institute for Materials Research, Tohoku University
 2-1-1, Katahira, Aoba-ku, Sendai 8577, Japan
 *not pictured
 Email: niinomi@imr.tohoku.ac.jp

Introduction

Biomedical implants are essentially foreign substances within the human body that must survive many years' exposure to demanding mechanical and physiological conditions. Despite these challenges, metal implants have been widely used to substitute for or rebuild hard tissues such as bones and teeth. Metal implants are particularly useful in applications where large loads are imposed, because the mechanical reliability (e.g., fatigue strength and toughness) of metals is much higher than those of ceramics and polymers. In fact, high mechanical reliability is one of the most important properties of the metals used for implants and general structural applications. As a result, around 80% of artificial hip joints, bone plates, spinal fixation devices, and artificial dental roots are currently produced from metal.¹ To achieve mechanical biocompatibility, metals used for implants must be mechanically harmonized with hard tissues. Young's modulus is a characteristic that describes the response of a material to stress and strain that can be used to understand mechanical biocompatibility. For example, while the Young's modulus of bone is approximately 10–30 GPa,² that of two commonly used metals for implants, SUS 316 L stainless steel and Ti-6Al-4V ELI titanium alloy, exhibit Young's moduli of around 200 and 110 GPa, respectively.³ As a result of this difference in Young's modulus, the load transferred between commonly used metallic implants and bone is non-homogeneous, thereby reducing stress stimulation of the bone. This is known as the stress shielding effect. Bone is likely to atrophy under such conditions, loosening the metallic implant and frequently re-fracturing the cortical bone (hereafter, bone). Metals whose Young's moduli are equal to that of the bone are believed to be ideal for fabricating metallic implants, and for mitigating the stress shielding effect.

SUS 316 L stainless steel, Co-Cr-Mo alloys, and titanium and its alloys are the most commonly utilized metallic biomaterials used in implant devices. SUS 316 L stainless steel and Co-Cr-Mo alloys are categorized as bio-tolerant while titanium and its alloys are categorized as bio-inert. Therefore, titanium and its alloys are considered the most biocompatible of all metallic biomaterials. Furthermore, the Young's moduli of titanium and its alloys are much smaller than other metallic biomaterials such as SUS 316 L stainless steel and Co-Cr-Mo alloys, for which the Young's

modulus is around 210 GPa.⁴ Titanium alloys are further categorized according to their phase constitution as α -, ($\alpha+\beta$)-, and β -type titanium alloys. Among these alloys, the Young's moduli of the β -type titanium alloys are much lower than those of α - and ($\alpha+\beta$)-type titanium alloys. β -type titanium alloys are advantageous from the perspective of preventing stress shielding; therefore, researchers are developing low Young's modulus β -type titanium alloys composed of non-toxic and non-allergenic elements for biomedical applications.

The rods used in spinal fixation devices are one example of low Young's modulus β -type titanium alloys used in implant devices that are attracting attention. Spring-back, the degree to which a metal returns to its original shape upon release is one important characteristic of materials used in implants. The degree of spring-back in a device is affected both by the strength and by the Young's modulus of the implanted material. While surgeons desire a higher Young's modulus (less spring-back), patients desire a lower Young's modulus (more spring-back). Consequently, it is necessary to satisfy the competing requirements of both surgeons and patients.⁵ For surgeons, the degree of spring-back in the rods should be as small as possible to minimize rod manipulability during operations. Several β -type titanium alloys having partially tunable Young's moduli recently have been developed to address this issue. One additional consideration is a phenomenon known as "aging back", the natural tendency for low Young's modulus β -type titanium alloys to revert to their predominant shape after long-term use. This tendency also damages spinal fixation devices and must, therefore, be suppressed as much as possible.

This paper focuses on research to address the mechanical biocompatibility of low Young's modulus β -type titanium alloys and reviews recent reports on this topic.

Design and Development of Low Young's Modulus β -type Titanium Alloys

The use of non-toxic and non-allergic alloying elements is a priority when designing biologically and mechanically biocompatible titanium alloys. A variety of data can be used to select the appropriate alloying elements, including cell viability, corrosion resistance, biocompatibility, and the rate of known human allergy to various pure metals and representative metallic biomaterials.⁶⁻⁹ Niobium (Nb), tantalum (Ta), and zirconium (Zr) are known as the most harmless titanium alloying elements,¹⁰ while nickel (Ni) in particular, is not added due to the fact that it poses a high risk of allergic reaction. After the identification of non-toxic and non-allergic alloying elements, the reduction of the Young's modulus remains the highest priority of materials development. There are a number of strategies in alloy design that can be used to reduce Young's modulus. For example, large amounts of Nb and Ta, both β -stabilizing elements, are added to titanium to fabricate β -type titanium alloys. A small amount of Zr is usually added because it dissolves in both the α - and

β -phases and increases the strength of the resulting alloy. The chemical composition of low-modulus Ti-Nb-Ta-Zr alloys is determined based on this concept. It is convenient to use the DV- X_c cluster-based d-electron alloy design¹¹ because it requires a minimum number of experimental samples to determine the chemical composition of alloys. We have used d-electron alloy design to develop Ti-29Nb-13Ta-4.6Zr, referred to as TNTZ, and to conduct further research and development on this alloy. We have also developed Ti-16Nb-13Ta-4Mo, Ti-29Nb-13Ta-4Mo, Ti-29Nb-13Ta-2Sn, Ti-29Nb-13Ta-4.6Sn, Ti-29Nb-13Ta-6Sn, and Ti-29Nb-13Ta and fundamentally evaluated the mechanical biocompatibility (i.e., the Young's modulus and mechanical properties) of the titanium alloys. Based on these analyses, we have determined that TNTZ demonstrated the best mechanical biocompatibility properties.¹⁰ Rack, *et al.*, simultaneously developed Ti-35Nb-7Zr-5Ta.¹² The Ti-36Nb-2Zr-3Ta-O alloy also has been developed for consumer applications and is expected to be used in medicine.¹³ The representative β -type titanium alloys used for biomedical applications are listed in Table 1.¹⁴

Table 1. Representative β -type titanium alloys for biomedical applications

β -type Titanium Alloys	ASTM Standard	ISO Standard	JIS Standard
Ti-13Nb-13Zr	ASTM F 1713	—	—
Ti-12Mo-6Zr-2Fe	ASTM F 1813	—	—
Ti-12Mo-5Zr-5Sn	—	—	—
Ti-15Mo	ASTM F 2066	—	—
Ti-16Nb-10Hf	—	—	—
Ti-15Mo-2.8Nb-0.2Si	—	—	—
Ti-15Mo-5Zr-3Al	—	ISO 5832-14	JIS T 7401-6
Ti-30Ta	—	—	—
Ti-45Nb	AMS 4982	—	—
Ti-35Zr-10Nb	—	—	—
Ti-35Nb-7Zr-5Ta (TNZT)	Task Force F-04.12.23	—	—
Ti-29Nb-13Ta-4.6Zr (TNTZ)	—	—	—
Ti-8Fe-8Ta	—	—	—
Ti-8Fe-8Ta-4Zr	—	—	—

Due to the high cost of rare-metal elements such as Nb, Ta, Mo, and Zr, low-modulus β -type titanium alloys recently have been proposed based on using lower-cost elements such as Fe, Cr, Mn, Sn, and Al. Examples of such alloys include Ti-10Cr-Al,¹⁵ Ti-Mn,¹⁶ Ti-Mn-Fe,¹⁷ Ti-Mn-Al,¹⁸ Ti-Cr-Al,¹⁹ Ti-Sn-Cr,²⁰ Ti-Cr-Sn-Zr,²¹ Ti-(Cr, Mn)-Sn,²² and Ti-12Cr.²³

A number of Ni-free titanium alloys have been developed that avoid the hazardous effects posed by Ni, and many of these materials exhibit super-elasticity. All β -type titanium alloys showing a single metastable β -phase and β -stability suitable for enhancing deformation-induced martensite transformation also show low Young's moduli. They are roughly categorized into four groups:

- Ti-Nb alloys²⁴⁻³⁶ including Ti-Nb, Ti-Nb-O, Ti-Nb-Sn, Ti-Nb-Al, Ti-22Nb-(0.5-2.0)O (at%), Ti-Nb-Zr, Ti-Nb-Zr-Ta, Ti-Nb-Zr-Ta-O, Ti-Nb-Ta-Zr-N, Ti-Nb-Mo, Ti-22Nb-6Ta(at%), Ti-Nb-Au, Ti-Nb-Pt, Ti-Nb-Ta, and Ti-Nb-Pd
- Ti-Mo alloys³⁷⁻⁴¹ including Ti-Mo-Ga, Ti-Mo-Ge, Ti-Mo-Sn, Ti-Mo-Ag, Ti-5Mo-(2-5)Ag (at%), Ti-5Mo-(1-3)Sn (at%), and the Ti-Sc-Mo alloys
- Ti-Ta alloys⁴² including Ti-50Ta, Ti-50Ta-4Sn, and Ti-50Ta-10Zr
- Ti-Cr alloys⁴³ including Ti-7Cr-(1.5, 3.0, 4.5)Al

Other alloys such as TNTZ,⁴⁴ Ti-7Cr-(1.5, 3.0, 4.5)Al super elastic and shape memory alloys, Gum Metal [Ti-25at% (Ta, Nb, V) + (Zr, Hf, O)],¹³ and Ti-9.7Mo-4Nb-2V-3Al⁴⁵ super-elastic alloys have also been developed.

Young's Modulus

The Young's moduli of representative α -, ($\alpha+\beta$)-, and β -type titanium alloys used for biomedical applications are shown in Figure 1. The Young's moduli of the as-solutionized β -type titanium alloys lies roughly between 60 and 80 GPa, also shown in Figure 1.

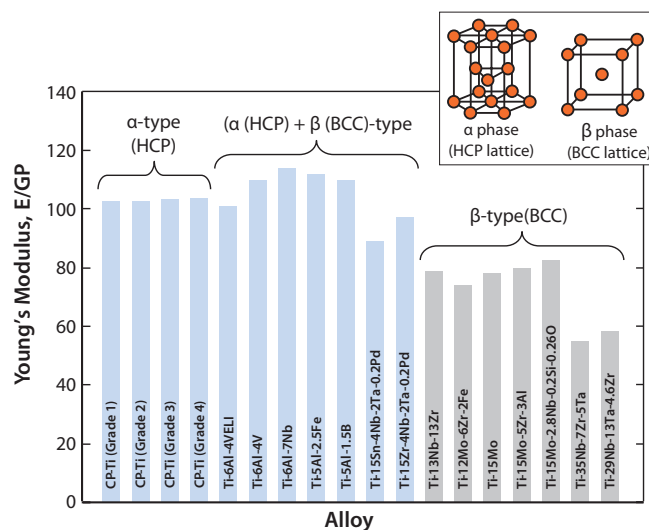


Figure 1. Young's moduli of α -, ($\alpha + \beta$)-, and β -type titanium alloys for biomedical applications

Since the mechanical strength of as-solutionized β -type titanium alloys is generally low, their mechanical strength can be improved by introducing secondary phases such as ω - and α -phases through heat or thermo-mechanical treatments. This process, known as precipitation strengthening, increases the Young's modulus. It has been reported that the Young's modulus of the heat-treated or thermo-mechanically treated TNTZ increases from 60 to 100 GPa, meaning that the Young's modulus of TNTZ tends to increase with increasing mechanical strength. It also means that TNTZ can be heat treated or thermo-mechanically treated to tune the Young's modulus from that of the β -type titanium alloy to that of the ($\alpha+\beta$)-type titanium alloy.

Further Reducing Young's Modulus

Reducing Young's Modulus by Tuning Crystal Growth Direction

It has been reported that the mechanical properties of TNTZ strongly depend on the direction of crystal growth.⁴⁷ Similarly, the Young's modulus of the β -type titanium alloy can also depend on the crystal growth direction. Severe cold-working β -type titanium alloys such as TNTZ can be used to form a texture showing preferentially aligned crystal growth. Therefore, it should be possible to grow textures consisting of preferentially oriented crystals of low Young's modulus β -type titanium alloys such as TNTZ. Figure 2⁴⁸ shows the Young's modulus of cold-rolled TNTZ plotted as a function of the cold-working ratio. The Young's modulus of the TNTZ cold-worked at 90% is around 56 GPa and that of the TNTZ not subjected to cold-working is around 65 GPa. The decrease in the Young's modulus induced by cold-working can be attributed to texture formation. The mechanical strength (including the tensile strength and 0.2% proof stress), on the other hand, increases while the ductility

(including elongation) decreases with the increasing cold-working ratio. The elongation, however, is relatively high as shown in Figure 3.⁴⁸

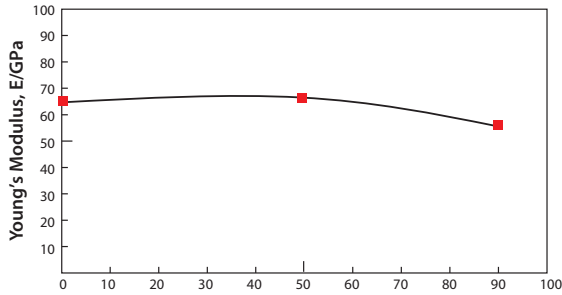


Figure 2. Young's modulus of TNTZ subjected to cold rolling as a function of cold working ratio.

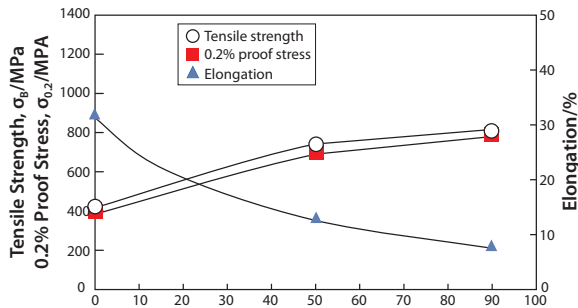


Figure 3. Tensile properties of TNTZ subjected to cold rolling as a function of cold working ratio.

Single crystals growing in a certain direction should show a low Young's modulus according to texture formation. Figure 4⁴⁹ shows the growth orientation dependence of the Young's moduli for the TNTZ single crystals growing between the $\langle 100 \rangle$ and $\langle 110 \rangle$ directions, which were calculated by converting the c_{ij} coordinates. θ denotes the angle measured from the $\langle 100 \rangle$ direction on the $\langle 110 \rangle$ zone axis. The Young's modulus of the TNTZ single crystals shows θ -dependent anisotropy; that is, the Young's modulus measured in the $\langle 100 \rangle$ direction, E_{100} , is approximately two times lower than that measured in the $\langle 111 \rangle$ direction, E_{111} , where E_{100} and E_{111} are the lowest and highest Young's moduli among those measured in all the directions, respectively. The lowest Young's modulus, E_{100} , for the TNTZ single crystal is only about 35 GPa, comparable to that for cortical bone. A Young's modulus this low may be effective in suppressing the stress shielding in bone.

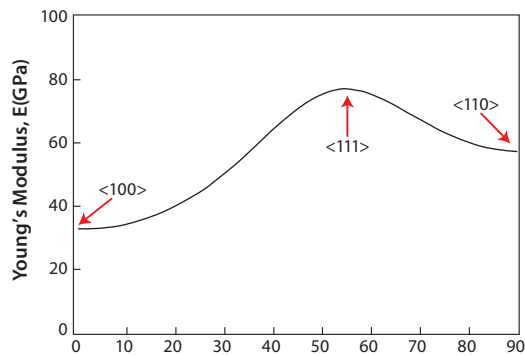


Figure 4. Young's modulus of TNTZ single-crystal in directions between $\langle 100 \rangle$ and $\langle 110 \rangle$.

Structurally Controlled Young's Modulus Reduction

Introducing porosity into titanium and its alloys is a very effective method of further reducing the Young's moduli of titanium and its alloys and it may enable the Young's modulus to be selectively tuned. A recent report compared the relationship between the Young's modulus and porosity of porous titanium produced from titanium powders of various diameters with those of bulk titanium.⁵⁰ According to the report, the Young's modulus of titanium with approximately 30% porosity was nearly equal to that of cortical bone. Using a titanium alloy that is less porous than bulk titanium, and whose Young's modulus is even lower than that of bulk titanium may produce an alloy with a Young's modulus equal to that of cortical bone. Properly sized pores also enhance bone conductivity. However, increasing titanium porosity drastically decreases titanium strength. The 0.2% proof stress of approximately 30% porosity titanium, which produces a Young's modulus equal to that of cortical bone, is below 100 MPa. The decrease in the strength of porous titanium can be prevented by combining the titanium with a biocompatible polymer. This can be achieved by pressing high-molecular-density polyethylene (HMDE) into porous titanium, enabling the polymer to penetrate.

Another method to fabricate polymer-infiltrated titanium⁵¹ involves immersing porous titanium (pTi) into a solution containing the methyl methacrylate monomer, thereby enabling the monomer to penetrate the titanium pores. The monomer-infiltrated porous titanium is then heated to polymerize the monomer. The strength of the porous titanium increases when combined with PMMA, as shown in Figure 5.⁵¹ While the tensile strength of the PMMA-infiltrated porous titanium is greater than that of the porous titanium, the Young's modulus of the PMMA-infiltrated porous titanium is nearly equal to that of the porous titanium (see Figure 6).⁵¹ The tensile strength of the PMMA-infiltrated porous titanium reportedly further increases while the Young's modulus remains unchanged when the PMMA-infiltrated porous titanium is treated with a silane coupling agent.

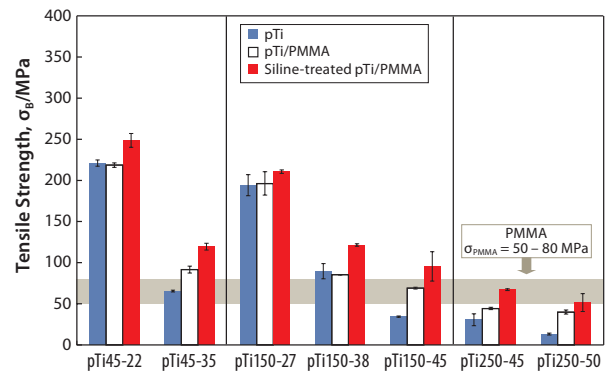


Figure 5. Tensile strength of pTi, pTi/PMMA, and Si-treated pTi/PMMA.

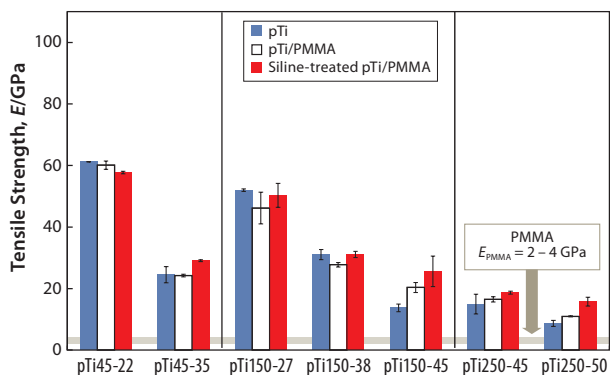


Figure 6. Young's moduli of pTi, pTi/PMMA, and Si-treated pTi/PMMA.

Biodegradable poly(L-lactic acid) (PLLA) can be used instead of PMMA to infiltrate the pores of porous titanium by modifying the process used for PMMA infiltration.⁵² Since PLLA is biodegradable, an agent used to enhance bone conductivity could be added to the PLLA in the porous titanium in order to facilitate controlled release of the agent into the body fluid.

Balance Between Maintaining Low Young's Modulus and Enhancing Strength or Endurance

It is important to increase strength while maintaining low Young's moduli of titanium alloys used for biomedical applications. These two factors are contradictory because a low Young's modulus is associated with weak bonding between atoms, while a high Young's modulus is associated with strong bonding. The Young's modulus of the β -phase (the main constituent of β -type titanium alloys) is generally lower than that of the α -phase (the main constituent of α - and $(\alpha+\beta)$ -titanium alloys) because the β -phase exhibits a body-centered cubic (BCC) crystal structure, where the atoms are roughly packed. The α -phase, however, has a hexagonal closed-packed (HCP) structure, with densely packed atoms. Therefore, it is more difficult to maintain the same Young's modulus for the solution-treated β -type titanium alloy compared to that of the as-prepared β -type titanium alloy because the strength of the as-prepared alloy can be increased through precipitation strengthening. Precipitation strengthening is used to strengthen the β -type titanium alloys while maintaining the lowest Young's modulus possible. When considering this, balance between maintaining a low Young's modulus and strengthening the alloy should be taken into account.

As previously shown, static strength properties such as the tensile strength of β -type titanium alloys (TNTZ) can be increased through work-hardening while maintaining a low Young's modulus. Severe-cold-working through cold rolling, swaging, or forging increases the static strength of the as-prepared β -type titanium alloy while maintaining the same Young's modulus as that of the solution-treated β -type titanium alloy, which exhibits the lowest Young's modulus.

Recently, severe plastic deformation has attracted much attention for its ability to increase the strength of metallic materials. Figure 7⁵³ shows the tensile properties of TNTZ subjected to high pressure torsion (HPT), a severe plastic deformation process, plotted as a function of N, the number of rotations, and those of the solution-treated and severe-cold-rolled TNTZ samples. HPT significantly increases the tensile strength, but decreases the elongation with increasing number of rotations. However, the elongation

remains fairly high. The Young's modulus of the HPT TNTZ remains almost constant, although it marginally decreases with increasing number of rotations, as shown in Figure 8.⁵³

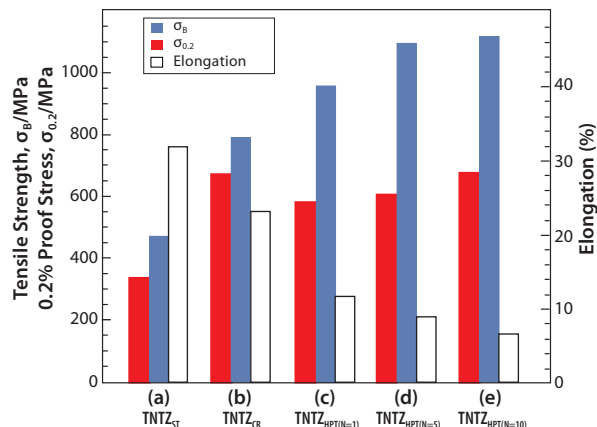


Figure 7. Tensile properties of TNTZ subjected to (a) solution treatment (TNTZ_{ST}), (b) severe cold rolling (TNTZ_{CR}), (c) HPT at a rotation number, N, of 1 (TNTZ_{HPT(N=1)}), (d) HPT at a rotation number, N, of 5 (TNTZ_{HPT(N=5)}) and (e) HPT at a rotation number, N, of 10 (TNTZ_{HPT(N=10)}).

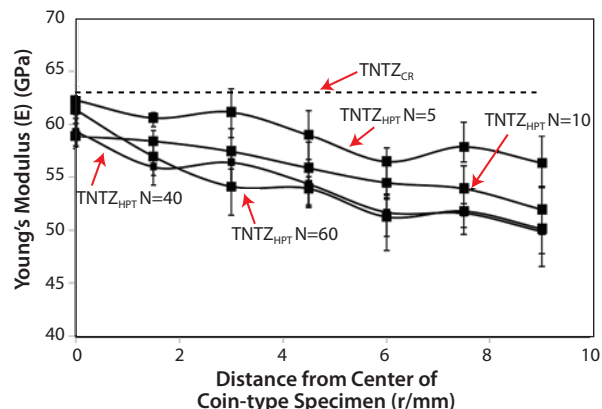


Figure 8. Young's moduli of TNTZ_{CR} and TNTZ_{HPT} at N= 5, 10, 40, and 60.

The dynamic strength, i.e., the fatigue strength of the severe-cold-worked TNTZ, was not higher than that of the solution-treated TNTZ.⁵⁴ However, the fatigue strength considerably improved when the solution-treated TNTZ was aged or when the TNTZ was thermo-mechanically processed including severe-cold-work and aging, as shown in Figure 9.⁵⁴ Aging produced the α - and ω -phase precipitates in the β -matrix. Therefore, precipitating the α - and/or ω -phases can significantly improve the fatigue strength. However, it also increases the Young's modulus because the Young's moduli of these phases are much higher than that of the β -matrix phase (see Figure 4).

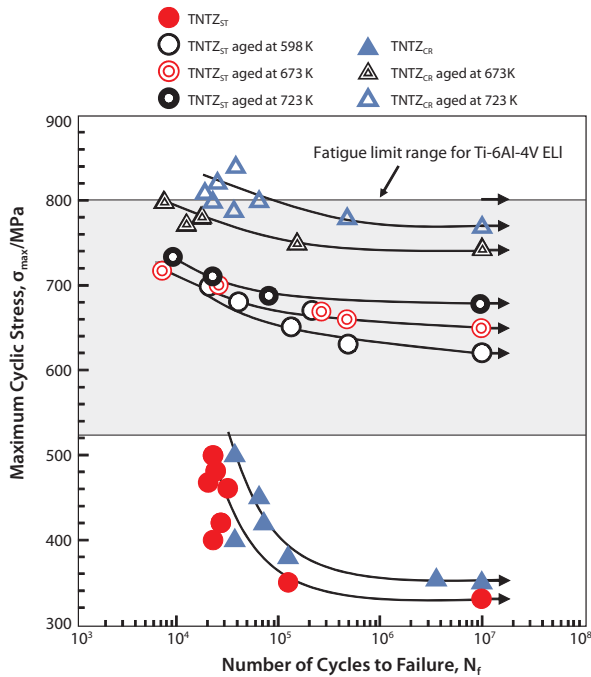


Figure 9. S-N curves of TNTZ conducted with aging at 598K for 259.2ks after ST (A_{598K}), aging at 673K for 259.2ks after ST (A_{673K}), aging at 673K for 259.2ks after CR (B_{673K}), and aging at 723K for 259.2ks after CR (B_{723K}), and fatigue limit ranges of hot rolled and cast Ti-6Al-4V ELI. CR indicates cold rolling.

Precipitating the ω -phase significantly increases the strength and the Young's modulus more than precipitating the α -phase; however, including the ω -phase also increases the brittleness of the alloy. Therefore, a small amount of ω -phase precipitate is considered optimal for improving the fatigue strength of TNTZ while maintaining a low Young's modulus. Aging TNTZ at fairly low temperatures for a short time induces a small amount of ω -phase to precipitate and is effective for this purpose. **Figure 10**⁵⁵ shows the Young's modulus of the solution-treated (ST) TNTZ, severe cold-rolled (CR) TNTZ, and the TNTZ aged at 573 K after solution treatment plotted as functions of aging time (AT). A tentative target for low Young's modulus β -type titanium alloys used for biomedical applications must be between 60 and 80 GPa. The Young's moduli of samples aged for approximately 10.8 ks remains below this target. When we evaluated fatigue properties plotted as S-N curves for ST, CR and TNTZ aged for 3.6 and 10.8 ks, we found that aging the TNTZ for 10.8 ks yields the most improvement in fatigue strength while maintaining the Young's modulus below 80 GPa.⁵⁵ Because aging the TNTZ for a short time at relatively low temperatures improves the fatigue strength while maintaining a low Young's modulus, precipitating the proper amount of the ω -phase in TNTZ is an effective method of improving the fatigue strength.

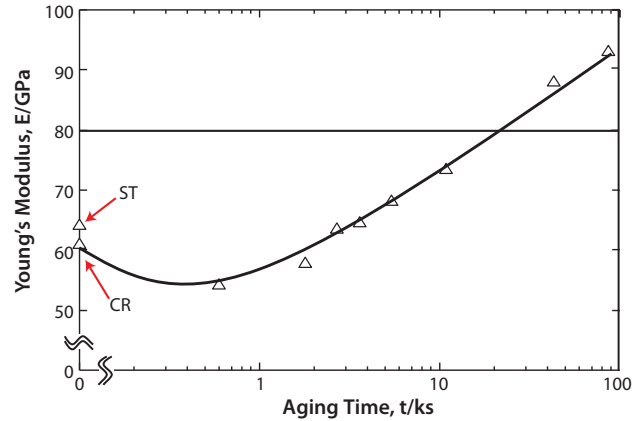


Figure 10. Young's moduli of ST, CR and TNTZ aged at 573K as a function of aging time: ST and CR indicate TNTZ subjected to solution treatment and severe cold rolling, respectively.

Adding a small amount of ceramic particles to the matrix is also an effective method of improving the fatigue strength of β -type titanium alloys while maintaining a low Young's modulus. The Young's moduli of cold-rolled TNTZ with TiB_2 or cold-rolled TNTZ with Y_2O_3 reportedly remained nearly constant around 60 GPa with increasing B and Y concentrations while the fatigue strengths of cold-rolled TNTZ after solution treatment containing 0.1 and 0.2% B or 0.2 and 0.5% Y was improved to that of Ti-6Al-4V ELI.⁵⁶

Bone Remodeling and Young's Modulus

Animal studies were conducted on Japanese white rabbits to determine how TNTZ, SUS 316 L stainless steel, and Ti-6Al-4V ELI implants affect bone remodeling.⁵⁷ Three-point bend tests were used to measure the Young's moduli of the TNTZ, Ti-6Al-4V ELI, and SUS 316 L stainless steel bone plates and found to be 58, 108, and 161 GPa, respectively. To do this, bone plates were implanted into fracture models using rabbit tibiae. Healing conditions were observed using X-ray photographs taken at regular intervals for 48 weeks after implantation. Next, both the tibiae and the bone plates were extracted, and bone formation was externally observed. Based on X-ray images taken from 4 to 18 weeks after implantation for each plate, it was observed that the cortical bone began to thin 7 weeks after the implantation of SUS 316 L stainless steel bone plate, almost completely disappearing 12 weeks after implantation. For the Ti-6Al-4V ELI bone plate, the cortical bone first showed signs of thinning 7 weeks after the implantation, almost completely disappearing 14 weeks after implantation. For TNTZ, the cortical bone initially appeared to thin 10 weeks after implantation, almost completely disappearing after 18 weeks.⁵⁷ Only the tibia implanted with the TNTZ bone plate showed an increase in the diameter of the tibia and in the double-wall structure of the intramedullary bone tissue, as shown in **Figure 11**.⁵⁷ The inner-wall bone structure represents the original cortical bone (i.e., the remaining old cortical bone) while the outer-wall bone structure represents the newly formed bone. The bone remodeling was the direct result of using a low Young's modulus bone plate. Therefore, using implants with a Young's modulus that is close to that of bone can be an effective method of preventing bone resorption and is expected to lead to good bone remodeling.

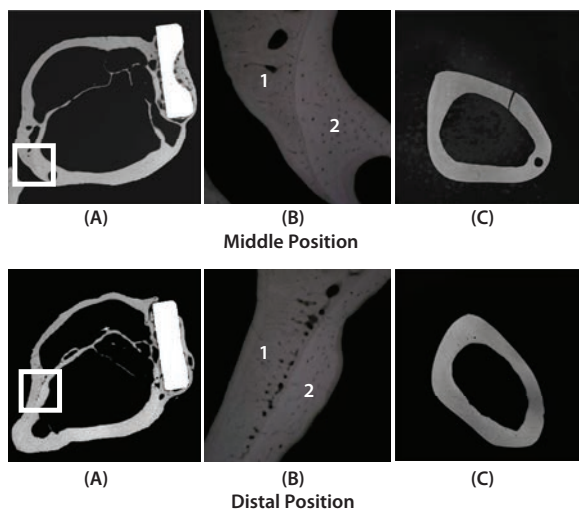


Figure 11. CMR (Contact Micro-Radiograph) images showing cross sections of fracture models implanted with and without bone plates made of TNTZ at middle position (above) and distal position (below) at 48 weeks after implantation. (A) Cross section of fracture model, (B) magnification of boxed area in (C) showing branched parts of bones that form the outer and inner sides of tibiae, and (C) cross sections of unimplanted tibiae.

Low Spring-back Alloys

Spinal fixation devices are a specific type of orthopedic implant that require a low Young's modulus to enable the formation of healthy bones.⁵⁸ However, during a spinal fixation operation, a surgeon must be able to bend the device in order to reproduce the physiological spinal curvature.⁵⁹ The operation is often performed within a limited space inside the patient's body; therefore, a large amount of spring-back can be problematic. Since a lower Young's modulus produces more spring-back, the Young's moduli of the titanium alloys used for spinal fixation devices must be sufficiently low to inhibit the stress shielding effect, yet high enough to suppress spring-back.⁶⁰ New titanium alloys whose pre-deformation Young's moduli are low but increase during deformation (i.e., self-tuning Young's moduli) have, therefore, been developed. Ti-Cr is the first such alloy developed and Ti-17Mo,⁶¹ Ti-30Zr-5Cr,⁶² Ti-30Zr-7Mo,⁶³ and Ti-30Zr-3Mo-3Cr⁶² have been subsequently developed. Ti-30Zr-5Cr⁶² and Ti-30Zr-3Mo-3Cr⁶² have been simultaneously developed for use as removable titanium alloys.

Young's moduli for a self-tunable titanium alloy, Ti-12Cr, and for solution-treated and cold-rolled TNTZ are shown in Figure 12.⁵ Note that Young's moduli of the Ti-12Cr and solution-treated TNTZ are similar (62–64 GPa). Since the cold-rolled TNTZ does not exhibit deformation-induced phase transformation, its Young's modulus shows almost no change. However, cold rolling increases the Young's modulus of Ti-12Cr due to the deformation-induced ω -phase transformation that occurs during cold rolling in Ti-12Cr. This is indicated in transmission electron microscopy (TEM) images.⁵ The formation of the ω -phase increases the Young's moduli of β -type titanium alloys,⁶⁴ which explains the increased Young's modulus of the cold-rolled Ti-12Cr.^{5,65,66} The densities of cells cultured in Ti-12Cr and other alloys for 86.4 ks (24 hr) also have been reported that Ti-12Cr exhibits the highest cell density.⁵

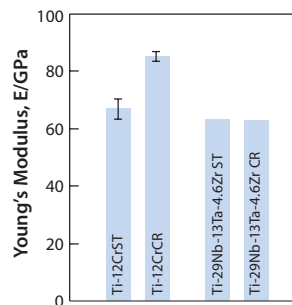


Figure 12. Young's moduli of Ti-12Cr and TNTZ subjected to solution treatment (ST) and cold rolling CR.

Decreasing the Cr content in Ti-(10–12)Cr alloys can decrease the β -(BCC)-lattice stability because Cr is a β -stabilizing element. This increases the amount of the ω -phase, which separates into the athermal and deformation-induced ω -phases formed during quenching and cold rolling stages, respectively. This suggests that lower Cr content may be beneficial for enhancing the ω -phase transformation in Ti-(10–12)Cr alloys. It is important to point out that suppressing the athermal ω -phase transformation is likely to increase the deformation-induced ω -phase transformation.⁶⁷ Suppressing the formation of the athermal ω -phase in low-Cr Ti-Cr alloys should not only achieve a low pre-deformation Young's modulus, but also increase the post-cold-rolling deformation-induced ω -phase transformation, thereby increasing the Young's modulus.

The addition of oxygen suppresses the formation of the athermal ω -phase in titanium alloys.^{68,69} For example, adding oxygen to Ti-Cr alloys increases their post-deformation Young's moduli.⁷⁰ Figure 13⁷⁰ shows the Young's moduli for solution-treated (ST) and cold-rolled (CR) Ti-(11, 12)Cr-(0.2, 0.4, 0.6)O alloys. The Young's moduli for alloys prepared with identical Cr content increase with increasing oxygen content. This is attributed to the oxygen-induced solid-solution-strengthening of the alloys and to the ω -phase transformation. Furthermore, the Young's moduli for Ti-11Cr-0.2O and Ti-12Cr-0.2O are almost identical, whereas Ti-12Cr-0.4O and Ti-12Cr-0.6O show slightly higher Young's moduli than those for Ti-11Cr-0.4O and Ti-11Cr-0.6O, respectively. This is reportedly because solution-treated Ti-11Cr-0.2O and solution-treated Ti-12Cr-0.2O still contain a small amount of the athermal ω -phase. Consequently, the competing formation of the athermal ω -phase, which can be suppressed by increasing the Cr content, stabilizes the lattice of the β -phase. This Cr-induced solid-solution strengthening of the alloys affects the Young's modulus. Conversely, the Cr-induced solid-solution strengthening of Ti-(11,12)Cr-(0.4, 0.6)O alloys primarily determines the Young's modulus because almost no athermal ω -phase forms; as a result, the solid solution-strengthening effect of Cr becomes the primary driver of the change in Young's modulus.

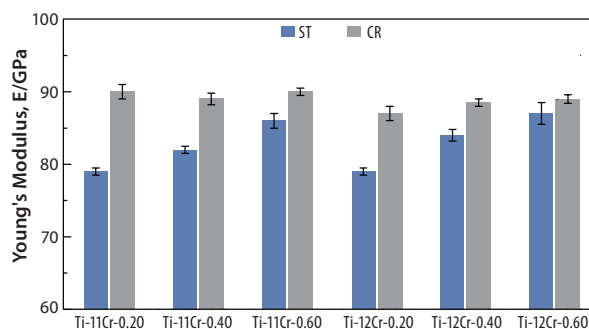


Figure 13. Young's moduli of Ti-(11, 12)Cr-(0.2, 0.4, 0.6)O alloys subjected to ST and CR.

The Young's moduli for cold-rolled alloys are always higher than those for solution-treated ones. Solution-treated Ti-11Cr-0.2O exhibits a Young's modulus below of 80 GPa, which is a much lower than those for SUS 316 L stainless steel, CP Ti, and Ti-6Al-4V ELI. Cold-rolled Ti-11Cr-0.2O exhibits a Young's modulus above 90 GPa. This change in the Young's modulus, which is the largest among all the materials examined, is desirable for satisfying the competing requirements of both surgeons and patients for spinal fixation applications. Figure 14⁷⁰ depicts the comparative profiles for the ratio of spring-back per unit stress plotted as a function of the applied strain for TNTZ, Ti-12Cr, Ti-11Cr-0.2O, and Ti-6Al-4V ELI. The ratio for Ti-11Cr-0.2O is always much lower than that for TNTZ, and is similar to that for Ti-6Al-4V ELI.

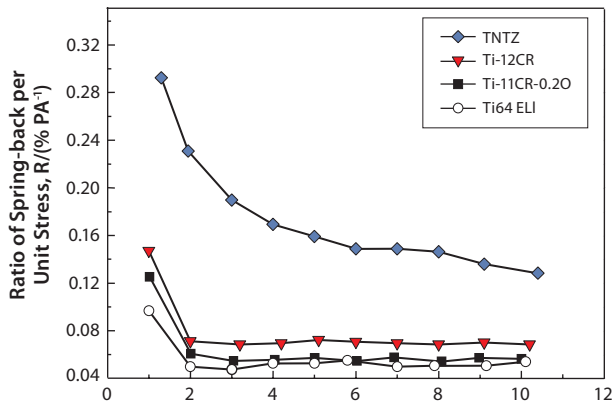


Figure 14. Ratio of spring-back per unit stress (R) as a function of applied strain for Ti-11Cr-0.2O, TNTZ, Ti-12Cr and Ti-6Al-4V ELI (Ti64 ELI) subjected to solution treatment.

Aging-back Characteristics

Implant rods must retain their shape over long durations. Screw-pullout-associated post-operative correction loss is one of the most serious concerns related to spinal fixation. A number of physicians report screw pullout associated with the loss of curvature in bent implant rods over time. This behavior, known as "aging-back", has even been observed for unloaded rods in an incubator at 310 K (37.0 °C).⁷¹ The aging-back of titanium is usually higher than that of stainless steel.⁷²

The aging-backs of variously heat-treated TNTZ rods and of rods composed of conventional biomaterials such as pure titanium (CP-Ti), Ti-6Al-4V (Ti-64), and SUS 316 L stainless steel (SUS316L) were evaluated and are shown in Figure 15.⁷³ The occurrence of aging-back increases exponentially with time for all the materials. Among the materials shown here, CP-Ti exhibits the worst aging-back while TNTZ-ST rod remains almost constant for over 3 months. Analysis of the temperature-dependence of these results indicates that the constituent phases contribute to the aging-back regardless of the chemical composition of the alloy. Bent rods undoubtedly age-back, and the degree of aging-back depends on the type of material. The microstructures of CP-Ti, Ti-64 and TNTZ-723K, and TNTZ-ST consist of a single HCP phase, mixed BCC and HCP phases, and a single BCC phase, respectively. Analysis of the material-dependence of these results indicate that aging-back is related to the type of crystal lattice. However, further investigations are needed to elucidate the details of this relationship.

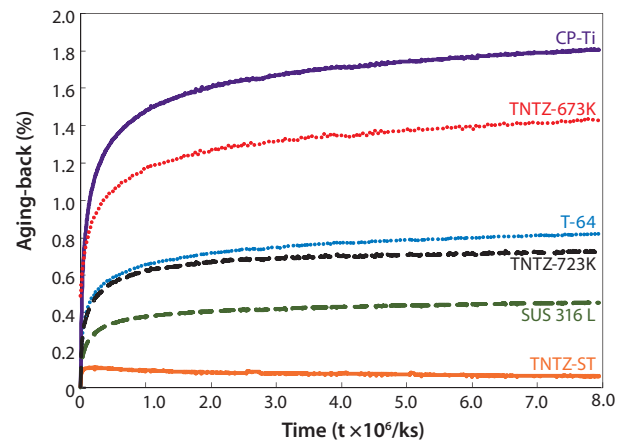


Figure 15. Aging-backs of as-solutionized TNTZ rod (TNTZ-ST), TNTZ rod subjected to aging treatment at 673K for 259.2 ks after solution treatment (TNTZ-673K) and TNTZ rod subjected to aging treatment at 723K for 259.2 ks after solution treatment (TNTZ-723K) in comparison with those of commercial pure Ti (CP-Ti), Ti-6Al-4V ELI (Ti-64) and stainless steel (SUS 316 L) as a function of time.

Summary

The results of animal tests clearly showed that the Young's modulus of the metallic biomaterial used for implant devices to replace failed hard tissue must be similar to that of the bone to effectively prevent bone resorption and promote good bone remodeling. However, the optimal Young's modulus required for achieving these outcomes is currently unclear and further research is necessary to determine it.

Alloy strength, ductility, and endurance must be increased while maintaining a Young's modulus close to that of the bone; however, it is somewhat difficult to simultaneously satisfy these requirements. Establishing an alloy design or process control that enables the addition of small amounts of elements as dispersed particles should enable these requirements to be more easily satisfied in the future.

Acknowledgments

This work was supported in part by a Grant-in-Aid for Scientific Research from the Japan Society for the Promotion of Science (JSPS) and by the inter-university cooperative research program "Innovative Research for Biosis-Abiosis Intelligent Interface" of the Ministry of Education, Culture, Sports, Science, and Technology (MEXT), Japan.

References

- Hanawa, T. *Metals for Medicine*; Japan Institute of Metals: Sendai, 2010.
- Niinomi, M.; Nakai, M.; Hieda, *Acta Biomater.* **2012**, *8*, 3888-3903.
- Niinomi, M. *Mater. Trans. A* **2002**, *33*(3), 477-486.
- Lemons, J. E.; *Perspectives on Biomaterials*; O. C. C. Lin, O. C. C.; Chao, E. Y. S. eds, Elsevier, New York, NY, **1986**, 1-13.
- Nakai, M.; Niinomi, M.; Zhao, X. F. et al.; *Mater. Lett.* **2011**, *65*, 688-690.
- Kawahara, H.; Ochi, S.; Tanetani, K.; Kato, K.; Isogai, M.; Mizuno, Y.; Yamamoto, H.; Yamaguchi, A. *J. Jpn. Soc. Dent. Appar. Mater.* **1963**, *4*, 65-75.
- Steinemann, S. G., *Evaluation of Biomaterials*; eds. G. D. Winter, J. L. Leray and K. de Groot: John Wiley & Sons Ltd., **1980**, 1-34.
- Niinomi, M. *Mater. Trans. A* **2002**, *33*(3), 477-486.
- Uggowitzer, P. J.; Bähr, W. -F.; Speidel, M. O., *Adv. Powder Metall. Part Mater.* **1997**, *3*, 18.113-18.121.
- Kuroda, D.; Niinomi, M.; Morinaga, M.; Kato, Y.; Yashiro, T., *Mater. Sci. Eng. A* **1998**, *243*, 244-249.
- Morinaga, M.; Yukawa, N.; Adachi, H., *Tetsu-to-Hagane* **1986**, *72*, 555-569.

- (12) Ahmed, T.; Long, M.; Silvestri, J.; Ruiz, C.; Rack, H. J. *Titanium'95*, eds. P. A. Blenkinsop, W. J. Evans and H. M. Flower: The Inst. Materials. **1996**; 1760-1767.
- (13) Saito, T.; Furuta, T.; Hwang, J. H.; Kuramoto, S.; Nishino, K.; Suzuki, N.; Chen, R.; Yamada, A.; Ito, K.; Seno, Y.; Nonaka, T.; Ikehata, H.; Nagasako, N.; Iwamoto, C.; Ikuhara, Y.; Sakuma, T. *Science* **2003**, *300*, 464-467.
- (14) Niinomi, M. *Biomaterials for Spinal Surgery*: Woodhead Publishing Ltd., 2012, 462-490.
- (15) Hatanaka, S.; Ueda, M.; Ikeda, M.; Ogawa, M. *Adv. Mater. Res.* **2010**, *89-91*, 232-237.
- (16) Ikeda, M.; Ueda, M.; Matsunaga, R.; Ogawa, M.; Niinomi, M. *Mater. Trans.* **2009**, *50*, 2737-2743.
- (17) Ikeda, M.; Ueda, M.; Kinoshita, T.; Ogawa, M.; Niinomi, M. (2012). *Mater. Sci. Forum* **2012**, *706-709*: 1893-1898.
- (18) Ikeda, M.; Ueda, M.; Matsunaga, R.; Niinomi, M. *Mater. Sci. Forum* **2010**, *654-656*, 855-858.
- (19) Ikeda, M.; Sugano, D. *Mater. Sci. Eng. C* **2005**, *25*, 377-381.
- (20) Ashida, S.; Kyogak, H.; Hosoda, H. *Mater. Sci. Forum* **2012**, *706-709*, 1943-1947.
- (21) Murayama, Y.; Sasaki S. *Univ. Res. J. Niigata Inst. Technol.* **2009**, *14*, 1-8.
- (22) Kasan, Y.; Inamura, T.; Kanetaka, H., et al., *Mater. Sci. Forum* **2010**, *654-656*, 2118-2121.
- (23) Nakai, M.; Niinomi, M.; Zhao, X. F., et al., *Mater. Lett.* **2011**, *65*, 688-690.
- (24) Kim, H. Y.; Ikehara, Y.; Kim, J. I.; Hosoda, H.; Miyazaki, S. *Acta Mater.* **2006**, *54*, 2419-2429.
- (25) Kim, J. I.; Kim, H. Y.; Hosoda, H.; Miyazaki, S. *Mater. Trans.* **2005**, *46*, 852-857.
- (26) Takahashi, E.; Sakurai, T.; Watanabe, S.; Masahashi, N.; Hanada, S. *Mater. Trans.*, **2002**, *43*, 2978-83.
- (27) Nitta, K.; Watanabe, S.; Masahashi, N.; Hosoda, H.; Hanada, S. Ni-free Ti-Nb-Sn shape memory alloys, *Structural Biomaterials for the 21st Century*, Niinomi, M.; Okabe, T.; Taleff, E. M.; Lesuer, D. R.; Lippard, H. E. (eds); TMS, Warrendale, PA, USA, **2001**, 25-34.
- (28) Hosoda, H.; Fukui, Y.; Inamura, T.; Wakashima, K.; Miyazaki, S.; Inoue, K., *Mater. Sci. Forum* **2003**, *426-432*, 3121-3125.
- (29) Inamura, T.; Hosoda, H.; Wakashima, K.; Miyazaki, S., *Mater. Trans.* **2005**, *46*, 1597-1603.
- (30) Kim, J. I.; Kim, H. Y.; Inamura, T.; Hosoda, H.; Miyazaki, S. *Mater. Sci. Eng. A* **2005**, *403*, 334-339.
- (31) Kim, H. Y.; Hosoda, H.; Miyazaki, S. *Collected Abstracts of the 2007 Spring Meeting of the Japan Institute of Metal and Materials*, **2007**, 91.
- (32) Ohmatsu, Y.; Kim, J. I.; Kim, H. Y.; Hosoda, H.; Miyazaki, S. *Collected Abstracts of the 2003 Spring Meeting of the Japan Institute of Metals and Materials*, **2003**, 144.
- (33) Al-Zain, Y.; Kim, H. Y.; Hosoda, H.; Nam, T. H.; Miyazaki, S. *Acta Mater.* **2010**, *58*, 4212-4223.
- (34) Kim, H. Y.; Sasaki, T.; Okutsu, K.; Kim, J. I.; Inamura, T.; Hosoda, H.; Miyazaki, S. *Acta Mater.* **2006**, *54*, 423-433.
- (35) Oshika, N.; Hashimoto, S.; Kim, J. I.; Kim, H. Y.; Ohmatsu, Y.; Hosoda, H.; Miyazaki, S. *Collected Abstracts of the 2003 Fall Meeting of the Japan Institute of Metals and Materials*, **2003**, 149.
- (36) Ping, D.; Mitarai, Y.; Yin, F. *Scr. Mater.* **2005**, *52*, 1287-1291.
- (37) Hosoda, H.; Hosoda, N.; Miyazaki, S. *Trans. MRS-J* **2001**, *26*, 243-246.
- (38) Kim, H. Y.; Ohmatsu, Y.; Kim, J. I.; Hosoda, H.; Miyazaki, S. *Mater. Trans.* **2004**, *45*, 1090-1095.
- (39) Hosoda, N.; Yamamoto, A.; Hosoda, H.; Miyazaki, S. *Collected Abstracts of the 2001 Fall Meeting of the Japan Institute of Metals and Materials*, **2001**, 401.
- (40) Maeshima, T.; Nishida, M. *Mater. Trans.* **2004**, *45*, 1096-1100.
- (41) Maeshima, T.; Nishida, M. *Mater. Trans.* **2004**, *45*, 1101-1105.
- (42) Ikeda, M.; Komatsu, S.; Nakamura, Y., *Mater. Trans.* **2004**, *45*, 1106-1112.
- (43) Ikeda, M.; Sugano, D.; Masuda, S.; Ogawa, M. *Mater. Trans.* **2005**, *46*, 1604-1609.
- (44) Niinomi, M.; Akahori, T.; Nakai, M.; Tsutsumi, H. *Mater. Trans.* **2009**, *50(7)*, 1704-1712.
- (45) Wu, M. H. *Proceedings of ASM Materials & Processes for Medical Devices Conf.*, 8-10 September, Anaheim, California, USA, **2003**, 343-348.
- (46) Niinomi, M.; Fukui, H.; Ogawa, M.; Toda, H. *Mater. Sci. Eng. C* **2005**, *25*, 248-254.
- (47) Sakaguchi, N.; Niinomi, M.; Akahori, T.; Takeda, J.; Toda, H. *Mater. Sci. Eng. C* **2005**, *25*, 363-369.
- (48) Niinomi, M. *Bull. Iron Steel Inst. Jpn.* **2010**, *15*, 661-670.
- (49) Tane, M.; Akita, S.; Nakano, T.; Hagihara, K.; Umakoshi, Y.; Niinomi, M.; Nakajima, H. *Acta Mater.* **2008**, *56*, 2856-2863.
- (50) Oh, H.; Nomura, N.; Hanada, S. *Mater. Trans.* **2002**, *43*, 443-446.
- (51) Nakai, M.; Niinomi, M.; Akahori, T.; Tsutsumi, H.; Itsuno, S.; Haraguchi, N.; Y. Itoh, Y.; Ogasawara, T.; Onishi, T.; Shindoh, T. *J. Mech. Behav. Biomed. Mater.* **2010**, *3*, 41-50.
- (52) Nakai, M.; Niinomi, M.; Ishii, D. *J. Mech. Behav. Biomed. Mater.* **2011**, *4*, 1206-1218.
- (53) Yilmazer, H.; Niinomi, M.; Akahori, T.; Nakai, M.; Tsutsumi, H. *Proc. PFAMXIII* **2009**, 1401-1410.
- (54) Niinomi, M.; Akahori, T. *Expert Review of Medical Devices* **2010**, *7*, 481-488.
- (55) Nakai, M.; Niinomi, M.; Oneda, T. *Metall. Mater. Trans. A* **2012**, *43*, 294-302.
- (56) Niinomi, M.; Nakai, M.; Song, X.; Wang, L. *Proc. PFAMXIX* **2011**, *2*, 817-827.
- (57) Sumitomo, N.; Noritake, K.; Hattori, T.; Morikawa, K.; Niwa, S.; Sato, K.; Niinomi, M. *J. Mater. Sci.: Mater. Medicine* **2008**, *19*, 1581-1586.
- (58) Narita, K.; Niinomi, M.; Nakai, M.; Akahori, T.; Oribe, K.; Tamura, T.; Kozuka, S.; Sato, S. *J. Jpn Inst Metals* **2008**, *72*, 674-678.
- (59) Steib, J. P.; Dumas, R.; Skalli, W. *Spine* **2004**, *29*, 193-199.
- (60) Nakai, M. *Materia Japan* **2010**, *49*, 437-440.
- (61) Zhao, X. F.; Niinomi, M.; Nakai, M. *Acta Biomater.* **2012**, *8*, 1990-1997.
- (62) Zhao, X. L.; Niinomi, M.; Nakai, M.; Miyamoto, G.; Furuhashi, T. *Acta Biomater.* **2011**, *7*, 3230-3236.
- (63) Zhao, X. L.; Niinomi, M.; Nakai, M. *J. Mech. Behav. Biomed. Mater.* **2011**, *4*, 2009-2016.
- (64) Matsumoto, H.; Watanabe, S.; Masahashi, N.; et al., *Metall. Mater. Trans. A* **2006**, *37*, 3239-3249.
- (65) Kasan, Y.; Inamura, T.; Kanetaka, H.; et al. *Mater. Sci. Forum* **2010**, *654-656*, 2118-2121.
- (66) Liu, H. H.; Niinomi, M.; Nakai, M.; Hieda, J.; Cho, K. *J. Mech. Behav. Biomed. Mater.* **2014**, *34*, 66-74.
- (67) Zhao, X. F.; Niinomi, M.; Nakai, M.; Hieda, J. *Acta Biomater.* **2012**, *8*, 2392-2400.
- (68) Williams, J. C.; de Fontaine, D.; Paton, N. E. *Metall. Trans. A* **1973**, *4*, 2701-2708.
- (69) de Fontaine, D.; Paton, N. E.; Williams, J. C. *Acta Metall.* **1971**, *19*, 1153-1162.
- (70) Liu, H. H.; Niinomi, M.; Nakai, M.; Hieda, J.; Cho, K. *J. Mech. Behav. Biomed. Mater.* **2014**, *30*, 206-213.
- (71) Burger, E. L.; Baratta, R. V.; King, A. G. S.; Easton, R.; Lu, Y. Solomonow, M.; Riemer, B. L. *Spine* **2005**, *30*, 375-379.
- (72) Andriy Noshchenko, A.; Vikas V. Patel, V. V.; Baldini, T.; Yun, L.; Emily M. Lindley, E. M.; Burger, E. L. *Spine* **2011**, *36*, 870-878.
- (73) Narita, K.; Niinomi, M.; Nakai, M.; Oribe, K. *Mater. Letters* **2012**, *86*, 178-181.

Precursors for Biomedical Alloys

Aluminum

For a complete list of available materials, visit aldrich.com/periodic.

Name	Purity	Description	Prod. No.
Aluminum	99.999% trace metals basis	evaporation slug diam. × L 6.3 × 6.3 mm	433705-25G
	99.7% trace metals basis	granular	518573-500G
	99.999% trace metals basis	foil thickness 1.0 mm	266957-27.2G
	99.999% trace metals basis	foil thickness 0.5 mm	266574-3.4G 266574-13.6G
	99.999% trace metals basis	foil thickness 0.25 mm	326852-1.7G 326852-6.8G
	≥99.99% trace metals basis	foil thickness 0.13 mm	326860-900MG 326860-3.6G
	≥99.999% trace metals basis	pellets	326941-25G
	99.99% trace metals basis	pellets	338788-50G
	≥99.95% trace metals basis	powder	202584-10G
	99.999% trace metals basis	rod diam. × L 3.0 × 100 mm	202576-10G
	99.999% trace metals basis	wire diam. 1.0 mm	266558-10.5G 266558-52.5G
	≥99.99% trace metals basis	wire diam. 0.58 mm	326887-7G 326887-35G
	99% trace metals basis	foil thickness 8 μm	733369-4EA
	99.99995% trace metals basis	ingot L × W 10 × 7 mm	773964-5EA

Chromium

For a complete list of available materials, visit aldrich.com/periodic.

Name	Purity	Description	Prod. No.
Chromium	99.995%	lumps	27050-100G-F
	99.995% trace metals basis	chips	374849-50G 374849-250G

Cobalt

For a complete list of available materials, visit aldrich.com/periodic.

Name	Purity	Description	Prod. No.
Cobalt	99.95% trace metals basis	foil thickness 1.0 mm	356891-5.6G 356891-22.4G
	≥99.99% trace metals basis	foil thickness 0.25 mm	266671-1.4G
	≥99.99%	foil thickness 0.1 mm	326380-8.8G
	99.95% trace metals basis	foil thickness 0.1 mm	356867-2.2G 356867-8.8G
	99.995% trace metals basis	granular	203076-5G 203076-25G
	≥99.9% trace metals basis	powder	266647-50G 266647-250G
	99.998% trace metals basis	rod diam. 5.0 mm	266663-3.4G
	99.95% trace metals basis	rod diam. 5.0 mm	398810-8.5G 398810-25.5G
	99.995% trace metals basis	wire diam. 1.0 mm	266701-1.4G

Molybdenum

For a complete list of available materials, visit aldrich.com/periodic.

Name	Purity	Description	Prod. No.
Molybdenum	≥99.9% trace metals basis	foil thickness 1.0 mm	357200-25.6G
	≥99.9% trace metals basis	foil thickness 0.1 mm	266922-10.2G
	≥99.9% trace metals basis	foil thickness 0.05 mm	514802-1.2G
	≥99.9% trace metals basis	foil thickness 0.025 mm	357227-5.8G
	99.99% trace metals basis	powder	203823-100G
	99.9% trace metals basis	powder	266892-100G
	≥99.99% trace metals basis	powder	366986-10G
	≥99.9% trace metals basis	powder	510092-50G 510092-250G
	99.95% trace metals basis	wire diam. 1.0 mm	266914-40G

Niobium

For a complete list of available materials, visit aldrich.com/periodic.

Name	Purity	Description	Prod. No.
Niobium	99.8% trace metals basis	foil thickness 0.25 mm	262781-32.1G
	99.8% trace metals basis	foil thickness 0.025 mm	268488-4.8G
	99.8% trace metals basis	powder	262722-25G 262722-100G

Tantalum

For a complete list of available materials, visit aldrich.com/periodic.

Name	Purity	Description	Prod. No.
Tantalum	≥99.9% trace metals basis	foil thickness 1.0 mm	262889-10.4G
	≥99.9% trace metals basis	foil thickness 0.5 mm	357251-20.8G
	≥99.9% trace metals basis	foil thickness 0.25 mm	262897-10.4G 262897-41.6G
	≥99.9% trace metals basis	foil thickness 0.05 mm	357243-8.4G 357243-18.9G
	≥99.9% trace metals basis	foil thickness 0.025 mm	262919-9G 262919-31G
	99.99% trace metals basis	powder	545007-10G
	99.9%	powder	692824-5G
	99.9% trace metals basis	powder	262846-25G 262846-100G
	≥99.9% trace metals basis	rod diam. 6.35 mm	262854-25G 262854-125G
	≥99.9% trace metals basis	rod diam. 3.2 mm	356980-6.5G
	≥99.9% trace metals basis	wire diam. 1.0 mm	262862-13G
	≥99.9% trace metals basis	wire diam. 0.5 mm	357006-3.3G

Titanium

For a complete list of available materials, visit aldrich.com/periodic.

Name	Purity	Description	Prod. No.
Titanium	≥99.99% trace metals basis (purity exclusive of Na and K content)	crystalline	305812-25G 305812-100G
	≥99.99% trace metals basis	evaporation slug diam. × L 6.3 × 6.3 mm	433667-4.8G
	99.7% trace metals basis	foil thickness 2.0 mm	369489-90G 369489-200G
	99.99% trace metals basis	foil thickness 0.5 mm	348805-1.4G
	99.99% trace metals basis	foil thickness 0.25 mm	267481-700MG
	99.7% trace metals basis	foil thickness 0.25 mm	267503-25.2G
	≥99.99% trace metals basis	foil thickness 0.127 mm	460397-1.5G
	99.7% trace metals basis	foil thickness 0.127 mm	348791-13G
	99.99% trace metals basis	foil thickness 0.1 mm	348813-280MG 348813-1.1G
	99.99% trace metals basis	foil thickness 0.05 mm	348821-2.2G
	99.98% trace metals basis	foil thickness 0.025 mm	348848-280MG 348848-1.1G
	99%	granular	89473-100G
	99.7% trace metals basis	powder (spherical)	578347-50G
	99.7% trace metals basis	powder	268496-50G
	99.98% trace metals basis	powder	366994-10G 366994-50G
	99.99% trace metals basis	rod diam. 6.35 mm	347132-7.2G
	99.7% trace metals basis	rod diam. 6.35 mm	266051-25G 266051-100G
	99.5% trace metals basis	sponge	268526-250G 268526-1KG
	99.99% trace metals basis	wire diam. 2.0 mm	348856-1.4G 348856-7G
	99.99% trace metals basis	wire diam. 1.0 mm	266035-350MG 266035-3.5G
	99.7% trace metals basis	wire diam. 0.81 mm	267902-23G
	99.99% trace metals basis	wire diam. 0.5 mm	348864-2.7G
	99.7% trace metals basis	wire diam. 0.25 mm	460400-2.2G 460400-11G
	99.99% trace metals basis	wire diam. 0.127 mm	266019-300MG

Vanadium

For a complete list of available materials, visit aldrich.com/periodic.

Name	Purity	Description	Prod. No.
Vanadium	99.7% trace metals basis	foil thickness 0.127 mm	357162-7.6G
	99.7% trace metals basis	foil thickness 0.25 mm	357170-15.2G
	99.7% trace metals basis	foil thickness 0.5 mm	266205-30G
	99.5% trace metals basis	powder	262935-10G 262935-50G
	99.7% trace metals basis	rod diam. 6.2 mm	266175-9G
	99.7% trace metals basis	turnings	262927-25G 262927-100G
	99.9% trace metals basis	pieces	774073-25G
	99.9% trace metals basis	powder	774065-5G

Zirconium

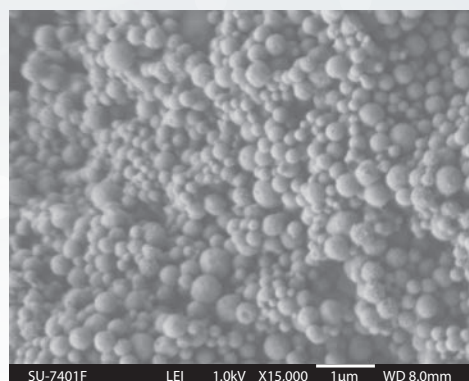
For a complete list of available materials, visit aldrich.com/periodic.

Name	Purity	Description	Prod. No.
Zirconium	99.98% trace metals basis	foil thickness 0.1 mm	419141-4.6G
	-	powder	403296-50G
	≥99% trace metals basis	rod diam. 6.35 mm	267724-20G
	≥99% trace metals basis	sponge	267651-100G
	99.5% trace metals basis (excluding Hf)	powder	756385-5G

FUNCTIONALIZED NANOPOROUS SILICA

Multifunctional Materials for Nanomedicine

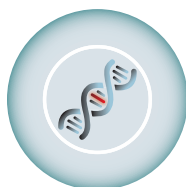
Aldrich® Materials Science offers a wide range of porous materials including nanoporous silica, nanoporous alumina, and functional nanoporous silica materials for biomedical applications. Fluorescent-labeled nanoporous silica particles aimed at diagnostics are a new range of tailored nanoporous products also offered.



Representative Materials

Name	Particle Size	Pore Size	Wavelength ($\lambda_{ex}/\lambda_{em}$)	Description	Prod. No.
Propylamine Functionalized Nanoporous Silica particles	<100 nm	4 nm	N/A	Surface functional group: Propylamine (-C ₃ H ₆ NH ₂)	749265
Propylthiol Functionalized Nanoporous Silica	<100 nm	4 nm	N/A	Surface functional group: Propylthiol (-C ₃ H ₆ SH)	749362
Propylcarboxylic Acid Functionalized Nanoporous Silica Particles	<100 nm	4 nm	N/A	Surface functional group: Propylcarboxylic Acid (-C ₃ H ₆ COOH)	749664
Propylcarboxylic Acid Functionalized Porphine-labeled Nanoporous Silica Particles	<100 nm	4 nm	416/670 nm	Surface functional group: Propylcarboxylic Acid (-C ₃ H ₆ COOH) Fluorescent loaded: meso-Tetra(4-carboxyphenyl) porphine(TCPP)	749680
Propylcarboxylic Acid Functionalized Fluorescein-labeled Nanoporous Silica particles	<100 nm	4 nm	488/520 nm	Surface functional group: Propylcarboxylic Acid (-C ₃ H ₆ COOH) Fluorescent loaded: Fluorescein isothiocyanate (FITC)	749699
Propylthiol Functionalized Fluorescein-labeled Nanoporous Silica particles	<100 nm	5 nm	488/520 nm	Surface functional group: Thiol Functional groups, (-C ₃ H ₆ SH) Fluorescent loaded: Fluorescein isothiocyanate (FITC)	749702
Propylthiol Functionalized Porphine-labeled Nanoporous Silica	<100 nm	4 nm	416/670 nm	Surface functional group: Thiol Functional groups, (-C ₃ H ₆ SH) Fluorescent loaded: meso-Tetra(4-carboxyphenyl) porphine(TCPP)	749710

For a complete list of mesoporous materials, visit aldrich.com/mesoporous



BIOMEDICAL



ELECTRONICS



ENERGY

BIO-INSPIRED “GREEN” SYNTHESIS OF NANOMATERIALS AND THEIR APPLICATIONS



Dr. Siddharth V. Patwardhan
Department of Chemical and Process Engineering
University of Strathclyde, 75 Montrose Street
Glasgow G1 1XJ, UK
Email: Siddharth.Patwardhan@strath.ac.uk

Introduction

Silica is a very popular inorganic nanomaterial used in a wide range of applications including fillers for rubber, catalyst supports, separation media, carriers in food and agriculture, and abrasive/antiskating agents in cosmetics. It is also widely believed to be an important material for biomedical applications for following reasons:

- Silica has been approved by the FDA as a material that is “Generally Recognized As Safe” and by the EU for use in cosmetics and food additives.¹
- Silica can be synthesized and modified using a number of well-established methods to produce a wide range of distinct varieties of silica (see below for details).¹⁻²
- Silica has excellent biodegradation/dissolution properties³ and dissolved silica is considered beneficial to bones.⁴

This article provides an introduction to the various types, chemistry, and traditional syntheses of silica, followed by an overview of the synthesis, properties, and applications of bio-inspired silica, including a perspective on potential applications.

Silica and Synthesis Methods

Although the term “silica” may suggest a single material type, in reality, the term represents a vast number of materials with distinct structures and properties. This includes silicas that are crystalline (minerals), amorphous, porous (both structured and unstructured pores), colloidal, as well as in a gel or other forms.⁵ However, each material type is differentiated in a number of ways, including through the position of the silicon and oxygen atoms, the sizes of the primary particle, secondary particles and aggregates, porosities, level of condensation/hydration (i.e., presence of silanol groups: Si–OH), and surface chemistry (e.g., distribution of surface silanols and surface charge). These seemingly subtle differences mainly arise from the method of synthesis, precursor chemistry, catalyst, solvent, finishing method (e.g., drying), and storage and can manifest themselves in significant ways.

A wide range of approaches have been developed for the preparation of silica nanomaterials, including mechanical methods (e.g., ball milling and attrition), physical techniques (e.g., sonochemical, sputtering, and microwave-assisted), chemical routes (vapor phase synthesis, precipitation, micelles, solvothermal, and sol-gel), and combinations thereof.⁶ In the past, we have witnessed three revolutionary technologies for the synthesis of silica, including the invention of “Stöber” synthesis for monodisperse nanoparticles (in 1968),⁷ as well as two methods for the synthesis of mesoporous silica, including MCM-41 (in 1992),⁸ and SBA-15 (in 1998).⁹ The Stöber route enabled the synthesis of monodisperse nanoparticles of controlled sizes, typically between 10–500 nm. Mesoporous silica synthesis, on the other hand, allowed access to porous materials with well-defined and tunable pores that has opened up a number of diverse applications. Collectively, these three papers received more than 22,000 citations, confirming their widespread impact. Mesoporous silicas (e.g., MCM-41 and SBA-15), colloidal Stöber silicas, and silica gels prepared via sol-gel methods are most relevant to biomedical applications, including toxicity research. Mesoporous silicas, in particular, have been of wide interest due to their high internal surface areas, large pore volumes, and unique customizable mesoporous structure.¹⁻² However, the process of mesoporous silica synthesis is typically complex, multistep, and energy intensive, involving harsh conditions including extremes of pH, high temperatures, and the use of highly toxic silica precursors.

Bio-inspired Silica

Biology exerts a remarkable level of control over fabrication of more than 60 distinct nanomaterials such as CaCO₃ (Aldrich Prod. No. 481807), Fe₃O₄ (Aldrich Prod. No. 518158), and silica produced under environmentally friendly conditions.¹⁰ Biology has identified a number of “clever” green routes to produce nanomaterials, and an understanding of the secrets of biological nanomaterials formation has the potential to lead to materials with novel applications and/or new technologies for nanomaterials production. The biological production of sophisticated nanomaterials encompasses most of the twelve principles of green chemistry and leads to exciting prospects.¹¹

Biogenic silica is highly sophisticated, hierarchically organized, and produced in a controlled fashion by microorganisms, animals, and plants formed under environmentally friendly and all-aqueous (“green”) conditions in ambient temperatures and pH. Biological and biochemical investigations have made substantial progress in understanding the mechanisms of biosilica formation (Figure 1). This process involves various specialized organic molecules such as proteins and enzymes that regulate the chemistry of silica formation *in vivo*.^{11a} For example, amines and amine-functionalized proteins have been identified, isolated, and characterized from silica forming microalga, while a family of specialized silicatein proteins have been discovered from a range of silica forming sponges.^{11a}

In order to further investigate molecular interactions between silica and biomolecules isolated from biosilica forming systems, a number of *in vitro* studies have been undertaken. These investigations involve the use of

advanced analytical tools, the use of model systems as well as modelling and simulations (Figure 1). Such *in vitro* experiments have produced a great deal of information on biosilicification, in addition to developing greener methods for the synthesis of tailorable silicas that are suitable for novel applications.

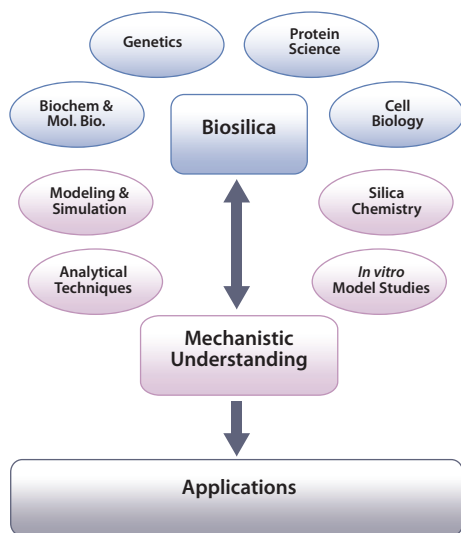


Figure 1. Scheme showing how the study of biosilica formation can lead to mechanistic understanding and generate applications. Image adapted from Patwardhan, *Chem. Commun.* 2011.^{11a}

Properties of Bio-inspired Synthesis and Bio-inspired Silica

Biologically inspired green synthesis provides significant improvements in comparison with existing materials and methods (Table 1). This includes (1) a one-pot, one-step route, offering substantial reductions in time and energy usage; (2) mild and facile processing using non-hazardous, environmentally benign chemicals, and (3) superior control of product properties to facilitate performance optimization. It is evident from Table 1 that mesoporous silica syntheses requires toxic precursors like tetraethoxysilane, long synthesis (2–6 days), high temperatures (>60 °C), and extremes of pH (needing specialized handling). In contrast, bio-inspired silica synthesis is far safer, routinely performed on bench-top at room temperature in water, and can be completed in 5 minutes.

During the last ten years, we have seen an exponential growth in research publications that cover biological and biologically inspired silica.^{11a} For example, researchers have unveiled mechanistic secrets of biosilica formation and how certain biomolecules play a crucial role in nanomaterial deposition through their chemistry and architecture. *In vitro* experiments on silica formation have enabled the development of bio-inspired green routes to silica by utilizing a wide variety of "additives" (analogues of biomolecules).¹³ These additives include a range of small to polymeric amines, polypeptides, proteins, and enzymes (selected examples are shown in Figure 2, an extensive list can be found in reference 11a). Furthermore, bio-inspired silica synthesis has been shown to be compatible with a wide variety of silica precursors (Figure 3) with unique features.¹⁴ As the understanding of the molecular interactions

between additives and nanomaterials are becoming more clear, increased control over the green synthesis of nanomaterials and their properties will become possible. For example, we have demonstrated the ability to tune particle size from <100 nm to 400 nm, surface area between 10–600 m²/g, as well as produce tailored morphologies (Figure 4).¹⁵ Various other advantages of the bio-inspired synthesis have been summarized in Table 2.

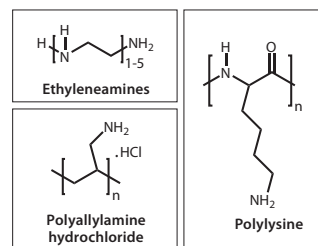


Figure 2. Structures of selected additives typically used in bio-inspired silica synthesis.

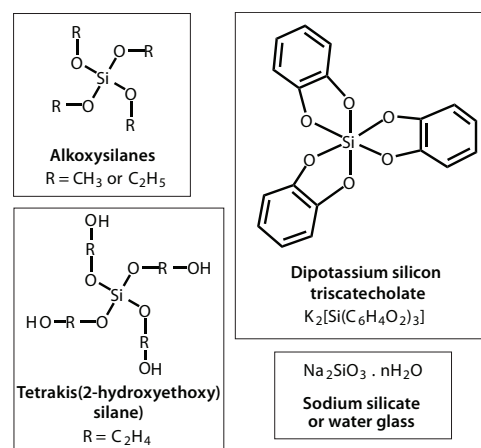


Figure 3. Chemistries of silica precursors typically used in bio-inspired silica synthesis.

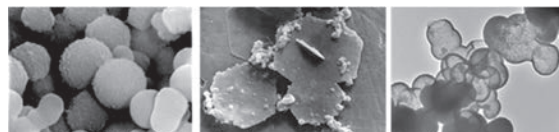
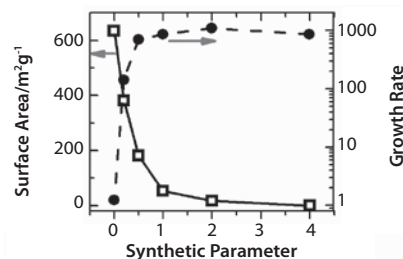


Figure 4. Examples of the ability of bio-inspired synthesis to control porosity, growth rates (top), and morphologies (bottom three images).

Table 1. Comparison of traditional methods with bio-inspired synthesis.¹²

Material	Reagents	Solvents	Reaction Conditions			By-products	Finishing
			Time (hr)	T (°C)	pH		
Mesoporous silica	TEOS, Surfactant	Water, Alcohol	48-144	60–100	~1 or ~10	Alcohol, Calcined surfactant	Calcination at 550 °C (6–24 hr)
Bio-inspired silica	Silicate & Additive	Water	0.08	20	7	NaCl	Drying at 100 °C (2 hr)

Table 2. Summary of properties that can be controlled in bio-inspired silica synthesis. Table adapted from Reference 11a.

Property	Nature of Control
Synthesis	Very slow to rapid (few seconds) precipitation
Morphology	Spherical particles, fibres, sheets, films, gels, hollow particles
Porosity	0–1,000 m ² g ⁻¹ (amorphous silica)
Composites	With biomolecules, drugs, polymers, quantum dots, catalysts, etc.

Applications

Only the basic principles of bio-inspired synthesis have been observed and potential applications have only been speculated. Examples of such potential applications are described below.

Biocatalysis

Bio-inspired routes for catalysis offer significant potential. Key advantages of this approach include mild processing conditions, facile, rapid and one-step procedures, and the potential to achieve high enzymatic activity and stability. This is a “doubly” green approach, since enzymatic processes are known to provide greener alternatives, while green immobilization methods eliminate further waste and pollution. A wide range of enzymes have been successfully immobilized on bio-inspired silica, including catalase, peroxidases, oxidases, lipases, and many others.¹⁶

The success of biocatalysis was demonstrated using lipase as a commonly used model of an industrially important enzyme.¹² Here, very high levels of lipase immobilization efficiencies (close to 100%) were reported. It was revealed that the enzyme retained its full activity; any apparent reduction in activity was due to mass transfer limitations and not enzyme deactivation. An important feature of bio-inspired synthesis, as illustrated in **Figure 4**, is the ability to tailor physical properties. This control over physical properties can be exploited to modulate biocatalyst performance. The enzymes immobilized using bio-inspired synthesis generally exhibit excellent reuse potential, very low levels of leaching, improved chemical and thermal stabilities, and sustained performance in continuous reactor operations. These properties enable their commercial utilization and, in particular, open up applications in the food and pharmaceuticals sectors.

Drug Delivery

The mild processing and biocompatibility of silica has led scientists to explore the ability of bio-inspired silica as a delivery vehicle for carrying cargo such as fluorescent dyes and drug molecules.^{11a} Although this is an emerging sector for applications of bio-inspired silica, one example stands out. Sano *et al.* reported the loading and successful release of an anticancer drug using bio-inspired silica.¹⁷ It was postulated that drug release occurs via hydrolysis and disintegration of silica in aqueous solutions; thus, slowly releasing the anticancer protein resulting in cancer cell death. The ability to control the chemical properties such as degree of hydration will prove important in the future exploitation of silica for use in drug delivery systems.

Environmental Decontamination

Bio-inspired silica is typically micro- and mesoporous, and its porosity can be tuned by careful control of synthetic conditions. These properties have been exploited in selective adsorption and removal of pollutants from air, and by extension, from water as well. For example, the extraction of formaldehyde from contaminated air streams has been reported using bio-inspired silicas. The method exploits the selective chemisorption of formaldehyde by silicas.¹⁸ The performance of this approach can easily rival existing sorbent technologies. When considering the synthesis cost

and time, as well as green implications when preparing silica materials, it is clear that bio-inspired silicas have the potential to provide an exciting new platform for adsorption and environmental remediation of volatile organic compounds.

Scalable Manufacturing and Future Applications

Scalability of the synthesis process is crucial to establish the viability of the industrial-scale production of bio-inspired silica. The scaling-up of a bench-top reaction is often not trivial for reasons such as the non-linear nature of both the scaling of laws governing transport phenomena (e.g., mixing) and the surface area-to-volume ratios. Furthermore, heterogeneous reactions (i.e., those commonly used for nanomaterial production) and most unit operations are scale-dependent. Recently, it has been reported that the synthesis of bio-inspired silica is scalable¹⁹ using a bench-top continuous flow system to achieve continuous production of bio-inspired silica. The ability of this process to manufacture catalysts and biocatalysts was also reported. Taking it further, a design for large-scale bio-inspired silica production (~40,000 tonnes per annum) was recently completed.²⁰

Detailed evaluation of the economic feasibility of this design and a comparison with existing industrial silica production processes were also conducted. This feasibility work presented a promising plant design for large-scale manufacturing of bio-inspired silica. This process would be significantly economical compared to current production; the payback period is reduced to 25% of that of the traditional process. Hence, the bio-inspired process shows great promise for industrial-scale development. Furthermore, the green process was estimated to reduce the manufacturing carbon footprint by over 90%, mainly by reduced energy requirements. These benefits, in addition to the potential for improved control of nanomaterial properties using bio-inspired processes, promises a very interesting future for the development of bio-inspired silica.

References

- Garcia-Bennett, A. E. *Nanomedicine* **2011**, *6*, 867.
- (a) Tang, F.Q.; Li, L.L.; Chen, D. *Adv. Mater.* **2012**, *24*, 1504; (b) Brinker, C.J.; Scherer, G.W. *Sol-Gel Science: The Physics and Chemistry of Sol-Gel Processing*; Academic Press: Boston, **1990**.
- (a) He, Q.J.; Shi, J.L.; Zhu, M.; Chen, Y.; Chen, F. *Micropor. Mesopor. Mater.* **2010**, *131*, 314; (b) Patwardhan, S.V.; Tilburey, G.E.; Perry, C. C. *Langmuir* **2011**, *27*, 15135.
- Carlisle, E.M. *Science* **1970**, *167*, 279.
- (a) Iler, R.K. *The Chemistry of Silica*; John Wiley & Sons: New York, **1979**; (b) Kendall, T. *Industrial Minerals* **2000**, March, 49.
- (a) Gleiter, H. *Prog. Mater. Sci.* **1989**, *33*, 223; (b) Knauth, P.; Schoonman, J. *Nanostructured materials*; Kluwer Academic Publishers: Boston, MA, **2002**.
- Stöber, W.; Fink, A.; Bohn, E. J. *Colloid Interface Sci.* **1968**, *26*, 62.
- Kresge, C.T.; Leonowicz, M.E.; Roth, W.J.; Vartuli, J.C.; Beck, J.S. *Nature* **1992**, *359*, 710.
- Zhao, D.Y.; Feng, J.L.; Huo, Q.S.; Melosh, N.; Fredrickson, G.H.; Chmelka, B.F.; Stucky, G.D. *Science* **1998**, *279*, 548.
- Biomineralization*; Mann, S.; Webb, J.; Williams, R. J. P., Eds.; VCH: Weinheim, **1989**.
- (a) Patwardhan, S.V. *Chem. Commun.* **2011**, 7567; (b) Anastas, P.T.; Kirchoff, M. M. *Acc. Chem. Res.* **2002**, *35*, 686.
- Forsyth, C.; Patwardhan, S.V. *J. Mater. Chem. B* **2013**, *1*, 1164.
- Patwardhan, S.V.; Clarson, S.J.; Perry, C.C. *Chemical Communications* **2005**, 1113.
- Patwardhan, S.V.; Raab, C.; Huesing, N.; Clarson, S.J. *Silicon Chem.* **2005**, *2*, 279.
- Belton, D.J.; Patwardhan, S.V.; Annenkov, V.V.; Danilovtseva, E.N.; Perry, C.C. *Proceedings of the National Academy of Sciences of the United States of America* **2008**, *105*, 5963.
- Forsyth, C.; Patwardhan, S.V. In *Bio-Inspired Silicon-Based Materials*; Zelisko, P.M., Ed.; Springer: in press.
- Sano, K.I.; Minamisawa, T.; Shiba, K. *Langmuir* **2010**, *26*, 2231.
- Ewlad-Ahmed, A.M.; Morris, M.A.; Patwardhan, S.V.; Gibson, L.T. *Environ. Sci. Technol.* **2012**, *46*, 13354.
- Patwardhan, S.V.; Perry, C.C. *Silicon* **2010**, *2*, 33.
- Drummond, C.; McCann, R.; Patwardhan, S.V. *Chem. Eng. J.* **2014**, *244*, 483.

Mesoporous Silicas

For a complete list of available materials, visit aldrich.com/mesoporous.

Name	Pore Size & Volume	Dimensions	Form	Prod. No.
Propylamine functionalized silica	pore size 4 nm	particle size 200 nm	nanoparticles	749265-5G
Propylcarboxylic acid functionalized silica	pore size 4 nm	particle size 200 nm	nanoparticles	749664-5G
	pore size 4 nm	particle size 200 nm	nanoparticles	749710-1G
	pore size 4 nm	particle size 200 nm	nanoparticles	749699-1G
Propylthiol functionalized silica	pore size 4 nm	particle size 200 nm	nanoparticles	749362-5G
	pore size 4 nm	particle size 200 nm	nanoparticles	749680-1G
	pore size 5 nm	particle size 200 nm	nanoparticles	749702-1G
Silica	pore size 4 nm	particle size 200 nm	nanoparticles	748161-5G
Silica, mesostructured	pore volume 2.31 cm ³ /g	spec. surface area 562 m ² /g	powder	560979-10G
	pore size 2-4 nm pore volume 1-2 cm ³ /g	spec. surface area 800-1000 m ² /g	powder	541036-5G 541036-25G
	pore size ~ 7.1 nm pore volume 0.91 cm ³ /g	spec. surface area ~750 m ² /g (BET)	powder	643637-5G 643637-25G
	pore size 2.1-2.7 nm pore volume 0.98 cm ³ /g	spec. surface area ~1000 m ² /g (BET)	powder	643645-5G 643645-25G

Mesoporous Materials

For a complete list of available materials, visit aldrich.com/mesoporous.

Name	Pore Size & Volume	Dimensions	Form	Prod. No.
Aluminosilicate, mesostructured	pore size 2.5-3 nm pore volume 1.0 cm ³ /g	spec. surface area 940-1000 m ² /g (BET)	powder	643653-5G 643653-25G
	pore volume 2.03 cm ³ /g	spec. surface area 605 m ² /g (BET)	powder	643629-5G 643629-25G
	average pore size 3.8 nm	particle size 5.65 μm (avg.)	powder	517747-5G
Aluminum oxide, mesoporous	average pore diameter 100 Å pore volume 0.5 cm ³ /g	particle size distribution 45 μm spec. surface area 150-250 m ² /g	powder	699640-5G 699640-25G
	mesoporosity 0.4-0.7 cm ³ /g microporosity 0-0.2 cm ³ /g	mesopore surface area ≥100 m ² /g spec. surface area >500 m ² /g (BET)	powder	702102-5G
	mesoporosity > 0.2 cm ³ /g	particle size 5 - 50 μm (SEM) spec. surface area >50 m ² /g (BET)	powder	702110-5G
	average pore diameter 64 Å total pore volume 0.342 cm ³ /g	particle size <500 nm (DLS) spec. surface area 150-250 m ² /g	nanopowder	699632-5G 699632-25G

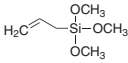
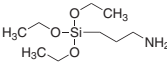
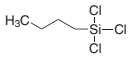
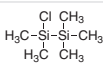
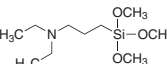
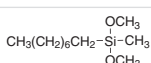
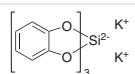
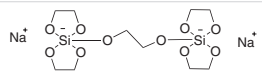
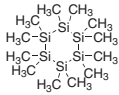
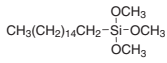
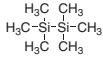
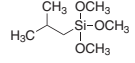
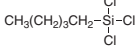
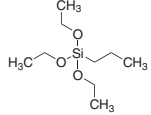
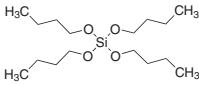
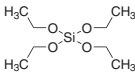
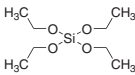
Silicon Nanomaterials

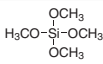
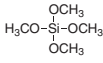
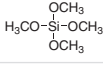
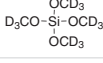
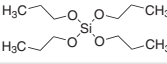
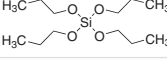
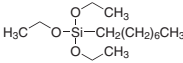
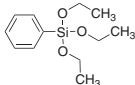
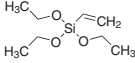
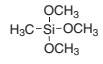
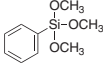
For a complete list of available materials, visit aldrich.com/nanopowders.

Name	Dimensions	Purity	Form	Prod. No.
Silica	primary particle size 12 nm (TEM) spec. surface area 175-225 m ² /g (BET)	99.8% trace metals basis	nanopowder	718483-100G
Silicon	particle size <100 nm (TEM)	≥98% trace metals basis	nanopowder	633097-10G 633097-25G
Silicon carbide	particle size <100 nm surface area 70-90 m ² /g	-	nanopowder	594911-100G 594911-250G
Silicon dioxide	particle size 10 - 20 nm (BET)	99.5% trace metals basis	nanopowder	637238-50G 637238-250G 637238-500G
	particle size 5 - 15 nm (TEM) surface area 590-690 m ² /g (TEM)	99.5% trace metals basis	nanopowder	637246-50G 637246-250G 637246-500G
	particle size <50 nm spec. surface area 75.5 m ² /g (BET)	99.99% trace metals basis	dispersion nanoparticles	701491-25ML 701491-100ML
Silicon nitride	particle size <50 nm (BET) BET surf. area >109.4 m ² /g	≥98% trace metals basis	nanopowder	634581-5G

Silica Solution Deposition Precursors

For a complete list of available materials, visit aldrich.com/solutiondeposition.

Name	Structure	Purity	Prod. No.
Allyltrimethoxysilane		≥98%	679267-50G
(3-Aminopropyl)triethoxysilane		99%	706493-20ML
Butyltrichlorosilane		≥98%	679224-50G
Chloropentamethyldisilane		97%	490407-5G
[3-(Diethylamino)propyl]trimethoxysilane		≥98%	679356-50G
Dimethoxy(methyl)octylsilane		≥95.0%, GC	68215-25ML
Dipotassium tris(1,2-benzenediolato-O,O')silicate		97%	468452-50G
Disodium [μ-(1,2-ethanediolato-O,O')]tetrakis(1,2-ethanediolato-O,O')disilicate		97%	465542-10G 465542-50G
Dodecamethylcyclohexasilane		-	437492-1G
Hexadecyltrimethoxysilane		≥85%, GC	52360-100ML 52360-500ML
Hexamethyldisilane		98%	217069-5G 217069-10G 217069-50G
Isobutyl(trimethoxy)silane		≥98%	679364-50G
Methyltrichlorosilane		≥98%, GC ≥99.99% (as metals)	679208-50G
Pentyltrichlorosilane		≥98%	679194-50G
Poly(carbodihydrosilane)		-	481068-5G
n-Propyltriethoxysilane		≥98%	679321-50G
Tetrabutyl orthosilicate		97%	T5702-100G
Tetraethyl orthosilicate		99.999% trace metals basis	333859-25ML 333859-100ML
		98%	131903-25ML 131903-250ML 131903-500ML 131903-1L 131903-2.5L 131903-4L

Name	Structure	Purity	Prod. No.
Tetramethylammonium silicate solution	$(\text{CH}_3)_4\text{N}(\text{OH}) \cdot 2\text{SiO}_2$	$\geq 99.99\%$ trace metals basis	438669-100ML 438669-500ML
Tetramethyl orthosilicate		$\geq 99.9\%$ trace metals basis	679259-50G
		$\geq 99\%$	341436-25G 341436-100G
		98%	218472-100G 218472-500G
Tetramethyl-d ₁₂ orthosilicate		-	393398-5G
Tetrapropyl orthosilicate		$\geq 98\%$	679240-50G
		95%	235741-25G 235741-100G
Triethoxy(octyl)silane		99.99% trace metals basis	679305-50G
Triethoxyphenylsilane		$\geq 98\%$	679291-50G
Triethoxyvinylsilane		$\geq 98\%$	679275-50G
Trimethoxymethylsilane		$\geq 98\%$	679232-50G
Trimethoxyphenylsilane		98%	679313-50G

NANOFLUIDS FOR BIOMEDICAL APPLICATIONS USING SPHERICAL IRON OXIDE MAGNETIC NANOPARTICLES FABRICATED BY HIGH-POWER PHYSICAL EVAPORATION



A. P. Safronov,^{1,2} I. V. Beketov,^{1,2} O. M. Samatov,¹ G. V. Kurlyandskaya,^{2,3*}

S. M. Bhagat,⁴ A. Larrañaga,⁵ I. Orue,⁵ R. Andrade⁵

¹Institute of Electrophysics, RAS, Amundsens St. 106, 620016, Ekaterinburg, Russia

²Ural Federal University, Lenin St. 51, 620000, Ekaterinburg, Russia

³Department of Electricity and Electronics, University of Basque Country UPV-EHU, Box 644, 48080 Bilbao, Spain

⁴FMR Group, Department of Physics, University of Maryland, College Park, MD 20742, USA

⁵SGiker, University of Basque Country UPV-EHU, Box 644, 48080 Bilbao, Spain

*Email: galina@we.lc.ehu.es

Introduction

Currently, magnetic nanoparticles (MNPs) are attracting a lot of attention because of the possibility of many novel applications, especially in biomedical research.^{1,2} To some extent the use of MNPs has been limited both by small production yields and by the difficulty of reproducibly manufacturing nanoparticles with specific properties. This lack of scale and reproducibility makes it very difficult to measure all of the critical parameters using MNPs from a single batch.³⁻⁶ In many cases, it is desirable to use multiple methods to measure the same property are desired.⁷ Here we review two preparation techniques that allow significantly enhanced production rates. First, we discuss the Electric Explosion of Wire (EEW) which yields high production rates (0.2 Kg/hr) and enables subsequent processing to obtain de-aggregated spherical MNPs of Fe, Fe₄₅Ni₅₅, Al₂O₃, TiO₂, ZrO₂, Fe₂O₃, Fe₃O₄, etc.⁸⁻¹⁰ Second, we used Laser Target Evaporation (LTE), a preparation technique capable of producing other interesting MNPs at the rate of 0.05 kg/h.¹¹⁻¹² The goal is to achieve the highest saturation magnetization and full de-aggregation leading to development of uniformly dispersed water-based ferrofluids for biomedical applications such as introduction into cells. Among various materials, magnetite invites particular attention because of its biocompatibility, high magnetization, high Curie point, and superparamagnetic response for fine particles.¹³

The review will provide a summary of some of the essential features of the EEW and LTE techniques followed by an outline of the subsequent physical and chemical processes used to obtain well-separated MNPs for incorporation into biomedically useful ferrofluids. Full details of our investigations have been published elsewhere.¹⁰⁻¹² In addition, we include results of structural characterization, transmission electron microscopy, magnetization, and ferromagnetic resonance measurements. These data lead us to conclude that we have manufactured magnetically uniform, nearly spherical particles of magnetite (EEW) and maghemite (LTE) that can be used to prepare useful ferrofluids.

Electric Explosion of Wire Technique

Figure 1A shows a schematic of the EEW method. Discharge of the high voltage source produces a current pulse of 10⁴ to 10⁶ A/mm² density which passes through the iron wire. The resulting energetic injection causes the energy density of the wire to considerably exceed the binding energy. The wire boils in a burst and a mixture of overheated vapor and boiling droplets scatter in the ambient gas. The wire explosion products expand in a cylindrical shape with a much larger density than that of the surrounding gas.^{8,10} While oxidation initially occurs only at the surface of the cylindrically shaped expansion of explosion products, oxygen penetrates inside the cylinder as it expands and promotes the process of burning and evaporation of the metal and the subsequent vapor condensation to yield oxide particles. Because the melting point of the oxides is much higher than that of metals, the size of the oxide particles that condense during oxidation is much smaller than that of the metal droplets as vapor concentration decreases. The size of the oxide MNPs can be adjusted broadly by delaying the burning process. This is due to the decrease in oxygen concentration and the concomitant increase in the speed of the particles. At higher speeds, the product presents a mixture of MNPs and micron-sized residual particles. Since a high proportion of microparticles can be undesirable for biomedical applications, a separation system using filters was created. This is accomplished through the inertial trap, shown in (4) of Figure 1A, located in the gas system of the EEW facility directly after the explosion chamber (1).

Transmission electron microscopy (TEM) images (Figure 1B) show that MNPs collected from the cyclone (shown as (5) in Figure 1A) are spherical. These so-called "cyclone MNPs" contain a coarser fraction and the presence of larger MNPs compared to samples collected from the filter (shown as (6) in Figure 1A). Both cyclone and filter samples were separated by centrifuging after which they were found to be almost identical with average mean diameters d_w of approximately 10 nm.

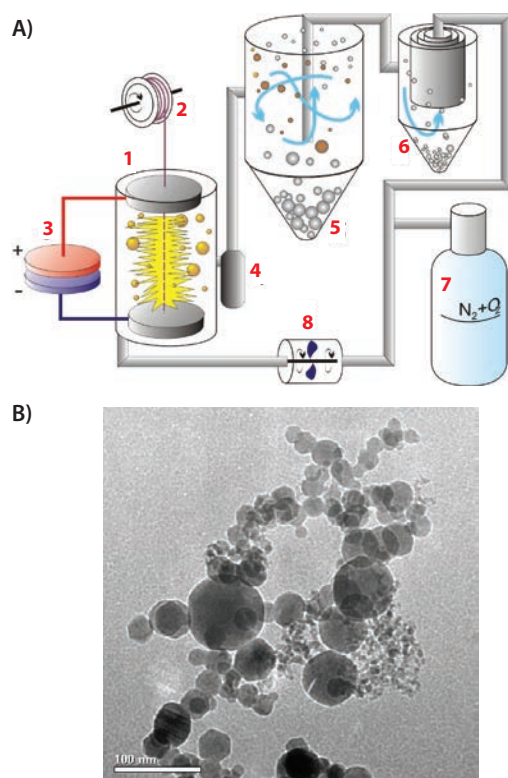


Figure 1. A) Installation for EEW—method to fabricate large batches of MNPs: 1—explosion chamber; 2—wire feeding mechanism; 3—high-voltage source; 4—inertial trap; 5—cyclone; 6—electric filter; 7—gas mixture deposit; 8—gas circulation fan. B) TEM image of EEW MNPs from the cyclone.

Figure 2 shows the X-ray diffraction (XRD) results of MNP studies performed using a DISCOVER D8 (Bruker) diffractometer operating with Cu-K α radiation ($\lambda = 1.5418 \text{ \AA}$). Quantitative analysis was performed using TOPAS-3 software. The average size of coherent diffraction domains was estimated using the Scherrer approach.¹⁴ **Figures 2A** and **2B** show the XRD spectrum of MNPs collected from the filter before and after separation by centrifugation. The typical cell parameter for magnetite was $a = 0.8396 \text{ nm}$. Slightly lower values of the cell parameters ($a = 0.8390$ and $a = 0.8368 \text{ nm}$ for MNPs from cyclone and filter before separation, respectively) indicated that the structure can be described as “defective spinel.” Although particles smaller than 30 nm predominated, a substantial number of particles with diameters above the superparamagnetic¹³ limit were still present. This minor fraction of large particles is responsible for the ferromagnetism; therefore, the separation of large particles is a requirement for the creation of nanofluids. Conventionally, this is performed using a liquid suspension of powder by sedimentation, which is based on Stokes’s law. Fractionization is the result of the more rapid sedimentation of the large particles compared to the small ones. Successful fractioning can be performed only when the particles are dispersed in liquid and move separately from one another. This necessary condition of de-aggregation is difficult to maintain. Aggregation during redispersion in liquid suspension is one of the main problems in processing air-dry nanoparticles.¹⁵ EEW iron oxide MNPs do not form stable suspensions in pure water even after ultrasonic treatment,

i.e., as-prepared air-dry MNPs are strongly aggregated and cannot be disassembled by shaking the water molecules. To address this, additional repulsive forces between MNPs must be introduced to overcome their mutual interactions. We performed specific studies on the factors controlling the colloidal stability of EEW MNPs in water suspensions. For this purpose, sodium citrate was selected as the electrostatic dispersant and stabilizer. We used zeta-potential measurements to determine the optimal concentration of electrostatic stabilizer, sodium citrate, and optimal pH to achieve stable EEW Fe₃O₄-water suspensions.¹⁶

Next, the magnetic properties of the MNPs were examined. $M(H)$ magnetization curves and magnetization as a function of temperature in zero-field-cooling (ZFC) and field-cooling (FC) processes were measured in the temperature range $5 \leq T \leq 300 \text{ K}$. Information about the size and anisotropy of the EEW Fe₃O₄ MNPs was obtained by the fitting of ZFC curves and assuming a coherent rotation of the magnetic moments inside each nanoparticle during the relaxation processes (Langevin formalism).¹⁷ A good fit was obtained, assuming a log-normal size distribution for the MNPs such that each nanoparticle has an average uniaxial anisotropy ($K \sim 1.2 \times 10^6 \text{ erg/cm}^3$) and no interactions between particles. The absence of hysteresis of $M(H)$ curves at room temperature and the shape of the hysteresis loops is typical of superparamagnetic systems (SPM). In SPM systems, at low temperatures the magnetization process in an increasing external field is associated with the rotation of the magnetic moment of each MNP toward the direction of the magnetic field. This process is energetically costly and results in high coercivity and remanence. With the increase of temperature, thermal fluctuations give rise to an SPM state, characterized by zero coercivity and a non-saturating behavior.

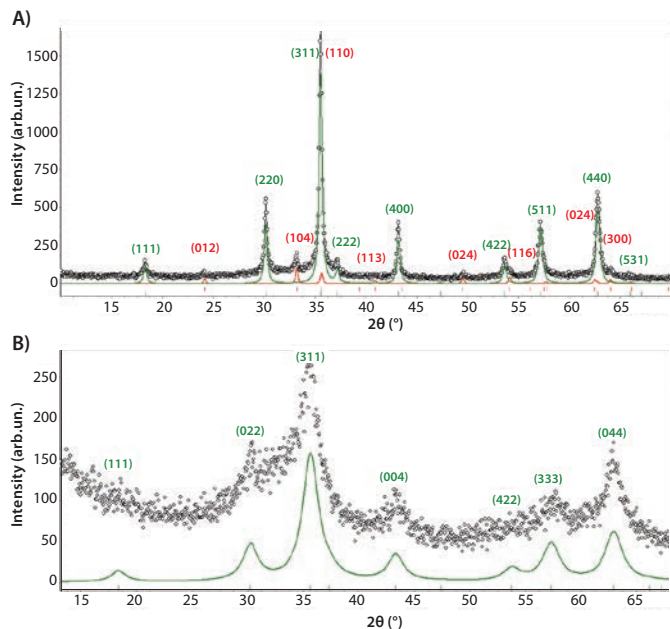


Figure 2. XRD patterns for EEW MNPs extracted from the filter before A) and after B) separation by centrifugation. Points—experimental data; lines—fitting results. Bragg positions are shown by the colored bars: red for hematite and blue for magnetite.

Laser Target Evaporation Technique

LTE MNPs are prepared using a device that includes a Ytterbium (Yb) fiber laser with a wavelength of $1.07\ \mu\text{m}$ (Figure 3A). To do this, a 65 mm diameter, 20 mm thick pellet target is pressed from commercially available coarse micron-sized iron oxide powder with a specific surface area of 0.5 to $1\ \text{m}^2/\text{g}$. The pellet target is annealed at $1,000\ ^\circ\text{C}$ for 1 hr in air prior to MNP fabrication by mounting it as part of the driving mechanism inside the evaporation chamber (shown as (1) in Figure 3). Both rotation and horizontal movement of the pellet were controlled. An optical system with 200 mm focal length and 0.45 mm diameter of the focal spot were used for focusing the laser beam onto the surface of the target. The driving mechanism provides a 20 cm/s beam scan rate on the target, ensuring uniform wear of the surface. A pulsed laser with a frequency of 5 kHz and pulse duration of $60\ \mu\text{s}$ favors the formation of fine MNPs with narrow particle size distribution. The working gas mixture of N_2 and O_2 is introduced into the evaporation chamber by a fan. Vapors of iron oxide that are driven out of the focal spot, condenses into MNPs, and are further carried out by the working gas into the cyclone (shown as (4) in Figure 3) and the fine filter (shown as (5) in Figure 3). The cyclone collected the coarse fraction of MNPs while the filter collects the fine fraction. TEM studies (Figures 3B and 4A) confirmed that the LTE MNPs are spherical in shape. Particle size distribution was found to be log-normal in the case of LTE MNPs with a mean diameter of 9.2 nm and dispersion of 0.368. MNPs fabricated by physical condensation in the vapor are found to aggregate. The proper choice of LTE parameters avoids the coalescence of the liquid droplets and prevents formation of non-spherical coarse agglomerates. However, due to the collision of physical surface forces, solid particles are inevitably aggregated in the gas phase. As a result, the iron oxide LTE MNPs contained a fraction of physical aggregates. To address this, the suspension was deaggregated by exhaustive ultrasonic treatment to achieve a constant average hydrodynamic diameter, followed by centrifuging. Two types of de-aggregated suspensions were obtained: MNPs-I (a water-based suspension without electrostatic stabilizer) and MNPs-II (a water-based suspension with sodium citrate as an electrostatic stabilizer, as shown in Figure 4B). The stoichiometric ratio $\text{Fe}^{2+}/\text{Fe}^{3+}$ in the MNPs is determined by redox potentiometric titration with potassium dichromate using an TitroLine automatic titrator (Schott Instruments). Titration is performed under an argon atmosphere to prevent oxidation of the Fe^{2+} in the air. The lattice constant of the crystalline phase is substantially smaller than that of stoichiometric magnetite, but larger than the lattice constant of $\gamma\text{-Fe}_2\text{O}_3$.

While a detailed description of the analysis of LTE MNPs magnetization behavior can be found elsewhere,¹² it is instructive to examine a few parameters. For example, the temperature dependence of the spontaneous magnetization in MNPs, $M_s(T)$, is due to thermal magnon excitation and can be described by the modified Bloch law:¹⁸ where $M(0)$ is the zero temperature magnetization, B is the Bloch factor and $\alpha=3/2$ for the material. The factor α is derived by fitting experimental values; these are strongly size dependent and approach the bulk limit for large powders with diameters on the order of hundreds of nm. In contrast to the bulk, the value of α in MNPs is $> 3/2$, increasing as the size of the MNP decreases due to the finite-size effect. Using the best fit for $M(T)$, the value $\alpha = 2.27 \pm 0.03$ is obtained for LTE MNPs. This value is consistent with the data for ferrite particles obtained by other techniques.¹⁸

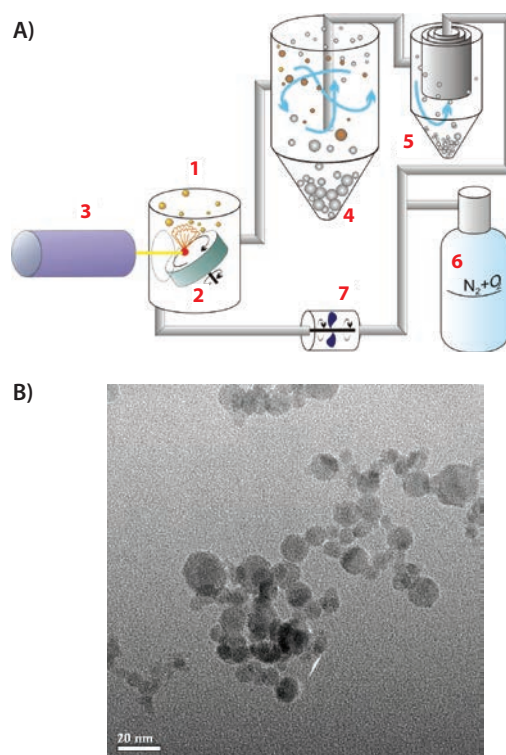


Figure 3. A) Installation for laser target evaporation method for fabrication of the iron oxide MNPs: 1–evaporation chamber; 2–target; 3–laser; 4–cyclone; 5–electric filter; 6–gas mixture deposit; 7–gas circulation fan. B) TEM image of LTE MNPs from the filter.

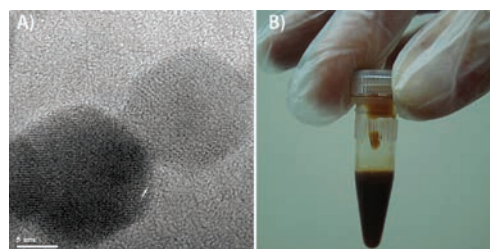


Figure 4. A) High resolution TEM image of iron oxide LTE MNPs. B) LTE MNP-based aqueous suspension with sodium citrate as an electrostatic stabilizer.

For practical purposes, both the saturation magnetization of a ferrofluid at room temperature as well as the de-aggregation state stability with respect to application of high magnetic field, are very important parameters. Figure 5 shows an example of $M(H)$ loop LTE MNPs-I water-based suspension with a maximum obtained concentration of 5 wt. % without an electrostatic stabilizer.

Ferromagnetic resonance (FMR) is a very informative technique for determining the sphericity of powder particles. This is because the field location of the line is strongly affected by deviations from spherical shapes. Accordingly, using techniques that we have developed over the years,^{4,9,12,19} we measured FMR at room temperature and 8.5 GHz for all of our powders, both as-prepared as well as when diluted with

non-magnetic talc. A typical signal is shown in **Figure 5B**. The following features are notable:

- Although rather wide (about 1 kOe) in every case, we observe only one resonance. This indicates that the grain material is magnetically uniform and homogeneous.
- For the given frequency, the line is centered at 3.1 ± 0.1 kOe. This is to be expected from a spherical ferromagnetic particle with negligible magnetocrystalline anisotropy.
- Dilution with talc reduces the linewidth only marginally, indicating that interparticle magnetic coupling is not the main source of the large linewidth. It is useful to recall that single crystal Fe_3O_4 films show FMR linewidths of about 1 kOe.

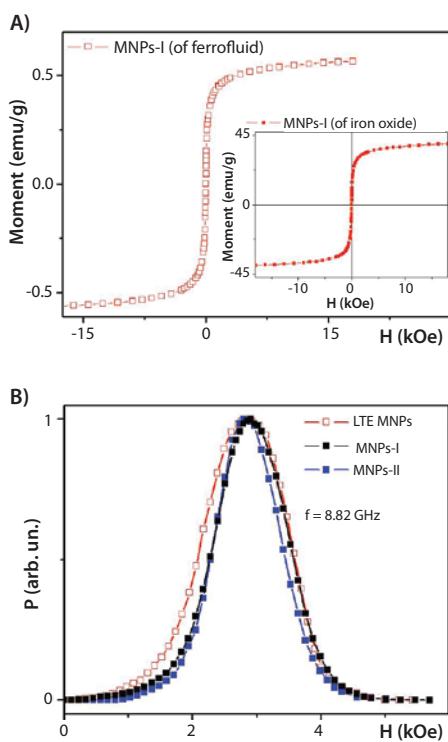


Figure 5. A) Hysteresis loop of LTE MNPs-I water-based suspension without electrostatic stabilizer; inset shows the same data recalculated for the unit mass of the iron oxide. B) Microwave losses at $f = 8.85$ GHz as a function of the external magnetic field for as-prepared LTE MNPs and dried MNPs corresponding to MNPs-II water-based suspension with electrostatic stabilizer and MNPs-I water-based suspension without electrostatic stabilizer.

As a final step, the biocompatibility of fabricated LTE MNPs-I and MNPs-II ferrofluids was tested. Two non-pathogenic types of yeasts were used: *Exophiala nigrum* (black yeasts) and its mutant strain (red yeasts) were selected for study of cytotoxicity and the possibility of MNPs accumulation in a living system (**Figure 6**). Two yeast strains were originally isolated from the Baikal and the Schumak river. These yeasts are interesting model systems as they play an important role in keeping equilibrium in the Baikal ecosystem. Liquid and gelatinous agar nutrient media were used for the cultivation of yeasts with controlled quantities of the ferrofluids. Magnetic measurements performed on dry yeast samples revealed more effective MNPs absorption from liquid nutrient than from gelatinized nutrient. Total reflection X-ray fluorescence (TXRF) using a Nanohunter spectrometer by Rigaku analyzed iron concentrations: yeasts grown in liquid medium had higher Fe concentrations (about 1,000 ppm for black yeasts) than yeasts grown in gelatinous agar medium (120 ppm for black yeasts). Cell morphology was studied by optical, scanning

(SEM), and transmission electron microscopies (TEM). In all cases for the selected conditions, no significant alterations of cell morphology were observed (**Figure 6**).

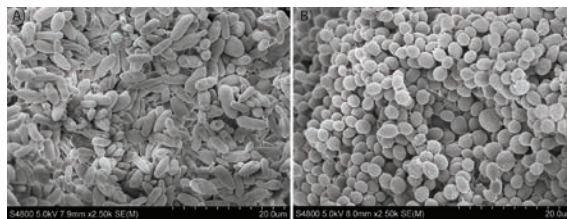


Figure 6. SEM microscopy of non-pathogenic strains: A) *Exophiala nigrum* (black yeasts) and B) its mutant strain (red yeasts).

Conclusions and Future Prospects

Ferrofluids possess the unique combination of fluidity and capability to be controlled by the application of an external magnetic field. Biomedical applications demand a large amount of de-aggregated magnetic nanoparticles in the form of water-based ferrofluids. High-power physical evaporation methods (EEW and LTE) are excellent candidates to ensure fabrication of fit-for-purpose ferrofluids. Recently, we have shown the possibility of measuring the concentration dependence of an LTE MNPs water-based suspension with an electrostatic stabilizer using a thin film giant magneto-impedance sensor.²⁰ In another case, the sensitivity of giant magneto-impedance sensitive elements was improved by covering the surface with polymer composite-containing EEP Ni water-based MNPs.²¹ These are interesting directions to follow.

Acknowledgments

This work was supported by CRDF and UB RAS grant 16991 and SAIOTEK-REMASEN grants. Selected studies were performed at SGiker services of UPV-EHU. We thank A.I. Medvedev, A.V. Bagazeev, A.M. Murzakaev, S.V. Komogortcev, J.P. Novoselova, N.S. Kulesh, T.P. Denisova and K.V. Zarubina for special support.

References

- (1) Huber, D.L., *Small*, **2005**, *5*, 482.
- (2) Llandro, J., Palfreyman, J.J., Ionescu, A., Barnes, C.H.W., *Med. Biol. Eng. Comput.*, **2010**, *48*, 977.
- (3) Jun, Y.-W., Seo, J.-W., Cheon, J., *Acc. Chem. Res.*, **2008**, *41*, 179.
- (4) Kurlyandskaya, G.V., Bhagat, S.M., Luna, C., Vazquez, M., *J. Appl. Phys.*, **2006**, *99*, 104308.
- (5) Baselt, D.R., Lee, G.U., Natesan, M., Metzger, S.W., Sheehan, P.E., Colton, R., *Bios. Bioelectr.*, **1998**, *13*, 734.
- (6) Kurlyandskaya, G.V., de Kos, D., Volchkov, S.O., *Russ. J. Nondestr. Test.*, **2009**, *45*, 377.
- (7) Grossman, J.H., McNeil, S.E., *Phys. Today*, **2012**, *65*, 38.
- (8) Kotov, Yu.A., *J. Nanoparticle Res.*, **2003**, *5*, 539.
- (9) Kurlyandskaya, G.V., Bhagat, S.M., Safronov, A.P., Beketov, I.V., Larrañaga, A., *AIP Adv.*, **2011**, *1*, 042122.
- (10) Bagazeev, A.V., Kotov, Yu.A., Medvedev, A.I., Azarkevich, E.I., Demina, T.M., Murzakaev, A.M., Timoshenkova, O.R., *Nanotechnologies in Russia*, **2010**, *5*, 656.
- (11) Beketov, I.V., Safronov, A.P., Bagazeev, A.V., Larrañaga, A., Kurlyandskaya, G.V., Medvedev, A.I., *J. All. Comp.*, **2014**, *586*, S483.
- (12) Safronov, A.P., Beketov, I.V., Komogortcev, S.V., Kurlyandskaya, G.V., Medvedev, A.I., Leiman, D.V., Larrañaga, A., Bhagat, S.M., *AIP Adv.*, **2013**, *3*, 052135.
- (13) Pankhurst, Q.A., Connolly, J., Jones, S.K., Dobson, J., *J. Phys. D*, **2003**, *36*, R167.
- (14) Scherrer, P., *Nachr Ges Wiss Göttingen*, **1918**, *26*, 98.
- (15) Hwang, Y., Lee, J.-K., Jeong, Y.-M., Cheong, S., Ahn, Y.-Ch., Kim, S.H., *Powder Technology*, **2008**, *186*, 145.
- (16) Beketov, I.V., Safronov, A.P., Medvedev, A.I., Alonso, J., Kurlyandskaya, G.V., Bhagat, S.M., *AIP Adv.*, **2012**, *3*, 022154.
- (17) Chantrell, R.W., Wohlfarth, E.P., *Phys. Stat. Sol. A*, **1985**, *91*, 619.
- (18) Hendriksen, P.V., Linderroth, S., Lindgard, P.A., *Phys. Rev. B*, **1993**, *48*, 7259.
- (19) Srinivasu, V.V., Lofland, S.E., Bhagat, S.M., Ghosh, K., Tyagi, S.D., *J. Appl. Phys.*, **1999**, *86*, 1067.
- (20) Yuvchenko, A.A.; Lepalovskii, V.N.; Vas'kovskii, V.O.; Safronov, A.P.; Volchkov, S. O.; Kurlyandskaya, G. V., *Techn. Phys.* **2014**, *59*, 230.
- (21) Lodewijk, K.J.; Fernandez, E.; Garcia-Arribas, A.; Kurlyandskaya, G.V.; Lepalovskii, V.N.; Safronov, A.P.; Kooi, J., *J. Appl. Phys.* **2014**, *115*, 17A323.

Iron Nanoparticles

For a complete list of available materials, visit aldrich.com/nanopowders.

Name	Dimensions	Purity & Concentration	Form	Prod. No.
Iron	particle size <100 nm	99.5% trace metals basis in mineral oil	dispersion	513423-5G
Iron-nickel alloy	particle size <100 nm (BET)	≥97%	nanopowder	677426-5G
Iron nickel oxide	particle size <50 nm (APS)	≥98% trace metals basis	nanopowder	637149-25G 637149-100G
Iron(II,III) oxide	particle size 50 - 100 nm (TEM)	97% trace metals basis	nanopowder spherical	637106-25G 637106-100G 637106-250G
Iron oxide(II,III), magnetic nanoparticles solution	avg. part. size 10 nm	5 mg/mL in toluene	solution	700312-5ML
	avg. part. size 5 nm	5 mg/mL in toluene	solution	700320-5ML
	avg. part. size 20 nm	5 mg/mL in toluene	solution	700304-5ML
Iron(III) oxide	particle size <50 nm (BET)	-	nanopowder	544884-5G 544884-25G
Iron(III) oxide, dispersion	particle size <110 nm (DLS)	20 wt. % in ethanol	nanoparticles	720712-100G
	particle size <100 nm (DLS)	20 wt. % in H ₂ O	nanoparticles	720704-100G

Magnetic Nanoparticles

For a complete list of available materials, visit aldrich.com/magnetic.

Name	Dimensions	Purity & Concentration	Form	Prod. No.
Barium ferrite	particle size <100 nm (BET)	>97% trace metals basis	nanopowder	637602-25G
Cobalt	particle size <50 nm (TEM)	≥99%	nanopowder	697745-500MG
Cobalt aluminum oxide	particle size <50 nm (BET)	≥99% trace metals basis (BET)	nanopowder	633631-25G
Cobalt(II,III) oxide	particle size <50 nm (TEM)	99.5% trace metals basis	nanopowder	637025-25G 637025-100G 637025-250G
Copper iron oxide	particle size <100 nm (BET)	98.5% trace metals basis	nanopowder	641723-10G
Copper zinc iron oxide	particle size <100 nm (BET)	98.5% trace metals basis	nanopowder	641650-10G 641650-50G
Dysprosium(III) oxide	particle size <100 nm (BET)	≥99.9% trace metals basis	nanopowder	637289-25G
	particle size <100 nm (BET)	≥99.9% trace metals basis 5 wt. % in H ₂ O	dispersion	639664-25ML
Holmium(III) oxide	particle size <100 nm (BET)	≥99.9% trace metals basis 5 wt. % in H ₂ O	dispersion	641863-25ML
	avg. part. size <100 nm (DLS)	≥99.9% trace metals basis	nanopowder	637327-10G 637327-50G
Iron oxide(II,III), magnetic nanoparticles solution	avg. part. size 5 nm	5 mg/mL in H ₂ O	dispersion	725331-5ML
	avg. part. size 10 nm	5 mg/mL in H ₂ O	dispersion	725358-5ML
	avg. part. size 20 nm	5 mg/mL in H ₂ O	dispersion	725366-5ML
Nickel	particle size <100 nm	≥99% trace metals basis	nanopowder	577995-5G
Nickel(II) oxide	particle size <50 nm (TEM)	99.8% trace metals basis	nanopowder	637130-25G 637130-100G 637130-250G
Nickel zinc iron oxide	particle size <100 nm (BET)	≥99% trace metals basis	nanopowder	641669-10G 641669-50G
Strontium ferrite	particle size <100 nm (BET)	99.8% trace metals basis	crystalline (hexagonal phase) nanopowder	633836-5G
Yttrium iron oxide	particle size <100 nm (BET)	99.9% trace metals basis	nanopowder	634417-10G
Zinc iron oxide	particle size <100 nm (BET)	>99% trace metals basis	nanopowder	633844-10G

Iron Wires

For a complete list of available materials, visit aldrich.com/magnetic.

Name	Purity	Description	Prod. No.
Iron	99.5%	wire reel, 250m, diameter 0.25mm, hard	GF58945078-1EA
	99.99+%	wire reel, 2m, diameter 0.13mm, hard	GF21695722-1EA
	99.99+%	wire reel, 2m, diameter 0.5mm, hard	GF48022152-1EA
	99.99+%	wire reel, 5m, diameter 0.025mm, as drawn	GF35663935-1EA
	≥99.99% trace metals basis	diam. 1.0 mm	266256-3.1G 266256-15.5G
	≥99.9% trace metals basis	diam. 1.0 mm	356824-6.2G 356824-31G
	≥99.9% trace metals basis	diam. 0.5 mm	356832-1.5G

ALDRICH
Materials Science

Now Available for Your iPad®

Material Matters
Download our free app!
aldrich.com/mm

SILVER NANOMATERIALS FOR BIOLOGICAL APPLICATIONS



Steven J. Oldenburg* and Aaron E. Saunders
nanoComposix, Inc., San Diego, California 92111
*Email: steve.oldenburg@nanocomposix.com

Introduction

Silver nanomaterials have unique physical, chemical, and optical properties that are currently being leveraged for a wide variety of biological applications. A resurgence of interest in the utility of silver as a broad-based antimicrobial agent has led to the development of hundreds of products that incorporate silver nanoparticles to prevent bacterial growth on surfaces. Additionally, silver nanoparticles have an optical color that is a function of their size and shape. The strong coupling of silver nanoparticles to specific wavelengths of incident light can be utilized to develop ultrabright reporter molecules, highly efficient thermal absorbers, and nanoscale “antennas” that can amplify the strength of the local electromagnetic field. Here we summarize how precise engineering of silver nanoparticle size and shape enables a wide range of biological applications.

Silver Nanomaterial Surface Chemistry, Morphology, and Optical Properties

The reaction conditions during silver nanomaterial synthesis can be tuned to produce colloidal silver nanoparticles with a variety of morphologies, including monodisperse nanospheres, triangular prisms, nanoplates, cubes, wires, and nanorods. For use in biological applications, the silver nanoparticle’s surface chemistry, morphology, and optical properties must be carefully controlled to obtain the desired functionality in the target environment.

Surface Chemistry

In many biological applications, it is desirable to tune colloidal stability in different buffers or media, or to vary particle binding or uptake via surface interactions. The surface chemistry of the particles (i.e., the binding strength, functional groups, and size of the capping agents) can be varied to provide an additional level of control over particle behavior. In aqueous media, many nanoparticles are electrostatically stabilized through the addition of charged species at the particle surface. The type and density of charges can be determined by measurement of the zeta potential of the colloid. Typically, the zeta potential of silver nanoparticles is negative due to surface-bound molecules such as citrate. By exposing the nanoparticle to more tightly coordinating ligands (often containing thiol

or amine functionality), new capping agents can bind to the surface and alter the chemical functionality and zeta potential of the nanoparticle. Replacing the citrate ions with short chain methoxy-terminated polyethylene glycol (mPEG) molecules provides a zeta potential near neutral, while coating the particles with branched polyethylenimine (BPEI) creates an amine-dense surface with a highly positive zeta potential.

Morphology and Optical Properties

Silver and other noble metal nanoparticles exhibit strong interaction with light, because the electrons on the metal surface undergo a collective oscillation when they are excited by light at specific wavelengths. This oscillation is known as surface plasmon resonance (SPR), and it causes the absorption and scattering intensities of silver nanoparticles to be much higher than identically sized non-plasmonic nanoparticles. The absorption and scattering properties of silver nanoparticles can be tuned by controlling the particle size, shape, and the local refractive index near the particle surface.

The optical properties of spherical silver nanoparticles are highly dependent on the nanoparticle diameter and uniformity, which can be controlled by carefully adjusting fabrication conditions to produce size-controlled particles with coefficients of variation (standard deviation of the diameter/mean diameter) less than 15% (Figure 1A). The *extinction* spectra of 10 sizes of silver nanoparticles at identical mass concentrations (0.02 mg/mL) are displayed in Figure 1B. Smaller nanospheres primarily absorb light with peaks near 400 nm, while larger spheres exhibit increased scattering, broader spectral peaks and peak intensities at longer wavelengths.

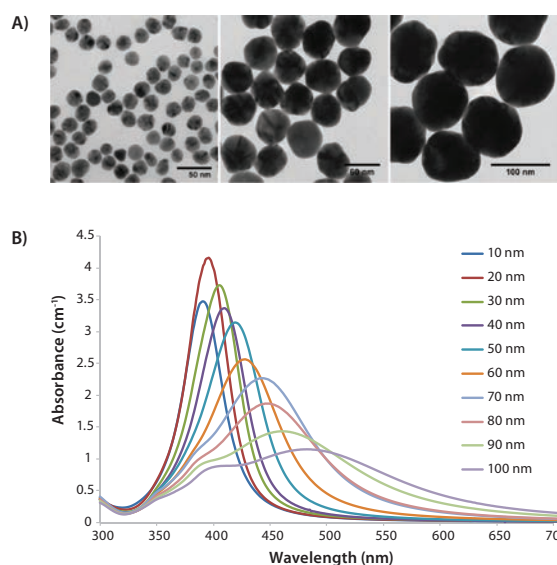


Figure 1. A) Transmission electron micrographs (TEM) of uniform 20 nm, 60 nm, and 100 nm diameter silver nanoparticles. B) Extinction (the sum of scattering and absorption) spectra of silver nanoparticles with diameters ranging from 10–100 nm at mass concentrations of 0.02 mg/mL.

Silver nanoplates are surface plasmon resonant (SPR) platelet-shaped nanoparticles (**Figure 2A**) that have extremely large absorbing and scattering cross-sections across the visible and near-IR regions of the spectrum. By precisely controlling the plate diameter and thickness, the nanoplate's optical resonance can be tuned to peak at specific wavelengths (550 nm–950 nm, **Figures 2B** and **2C**). Nanoplates have applications in Surface-Enhanced Raman Scattering (SERS), photovoltaics, molecular detection, and photothermal-based therapies.

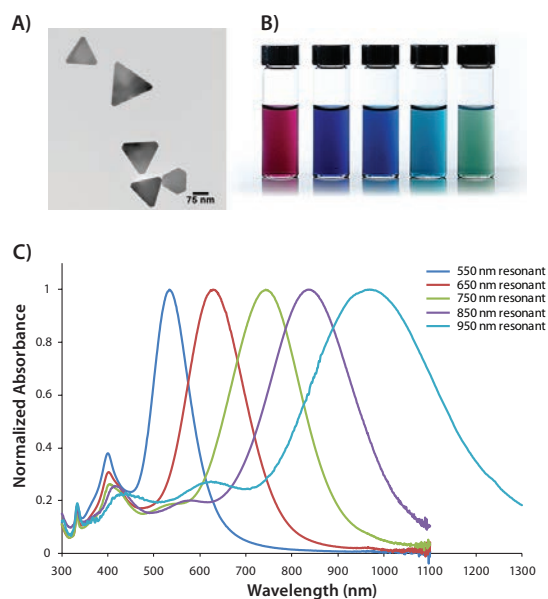


Figure 2. A) Transmission electron microscope (TEM) image of silver nanoplates. B) Dispersions of nanoplates exhibit colors that reflect the ability to tune the plasmon resonance of the nanoplates across the visible and near-infrared portion of the spectrum (C).

Surface-enhanced Spectroscopies

Other applications for silver nanoparticles in biological applications are based on utilizing the enhanced electromagnetic field on the surface and near the surface of the silver nanoparticle. At the plasmon resonant wavelength, the silver nanoparticles act as nanoscale antennas, increasing the intensity of the local electromagnetic field.

One spectroscopic technique that benefits from enhanced electromagnetic fields is Raman spectroscopy, where molecules can be identified by their unique vibrational modes. While intrinsic Raman scattering of photons from molecules is weak and requires long measurement times to obtain a Raman spectrum, Surface Enhanced Raman Scattering (SERS) from molecules near the surface of plasmonic metal nanoparticles offers greatly enhanced Raman signals. The SERS effect can enhance the Raman scattering of bound molecules by as much as 14 orders of magnitude, allowing for the detection of even single molecules.^{1,2} The enhancement is driven by the high electric field intensities (or "hot spots") created at locations on the nanoparticle surface and is, therefore, highly dependent on the nanoparticle geometry, surface features, and the specific position of the molecule. Metal nanoparticles exhibiting SERS from associated molecules (SERS nanotags) have been used as labels in a range of biomedical applications and platforms including immunoassays, nucleic acid sequence detection, *in vitro* cellular imaging, *in vivo* imaging, and flow cytometry.

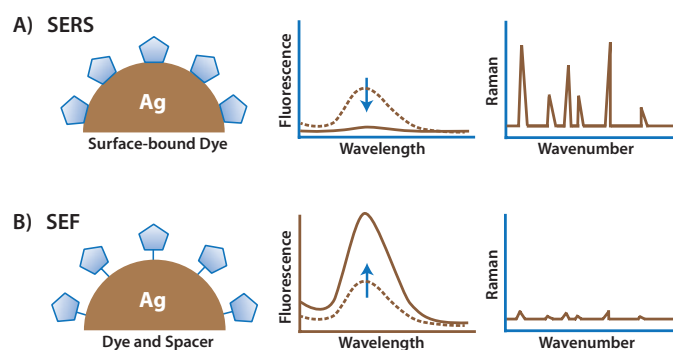


Figure 3. A) An organic fluorophore attached directly to a metal substrate typically has quenched fluorescence but a strong surface enhanced Raman spectrum (SERS). B) Spacing the fluorophore off of the metal surface results in surface enhanced fluorescence (SEF).

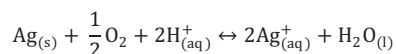
The increased localized field extends beyond the surface of the nanoparticle and, by placing a fluorophore a short distance away from the surface of a silver nanoparticle, gives rise to a phenomenon known as surface enhanced fluorescence (SEF). SEF was first observed in the 1970s and can enhance the fluorophore emission intensity by orders of magnitude.³ The enhancement of the fluorophore can be attributed to two effects: 1) the focusing of the incoming light due to the large absorption and scattering cross-sections of the plasmonic particle, and 2) a decrease in the fluorescence lifetime of the fluorophore that allows the excited state to return to the ground state at a higher frequency. Collectively, these two phenomena mitigate two drawbacks common to organic dye molecules: 1) the low absorbance cross section of molecules, and 2) a slow cycle time for excitation and emission per molecule. In order to maximize the fluorescence enhancement of a fluorophore, the optical properties of the metal nanoparticle and the geometry of the SEF nanotag must be carefully engineered by precisely controlling the metal particle size, shape, and composition as well as the distribution of the fluorophore near the particle surface.

A schematic of the different attachment strategies necessary to achieve optimal SERS and SEF effects with a dye molecule is shown in **Figure 3**. Attaching a dye molecule to a metal nanoparticle typically results in quenching the emission due to energy transfer between the excited state of the fluorophore and the electronic states of the metal. In this case, the Raman spectrum of the molecule is strongly enhanced due to the high electromagnetic field at the surface of the particle (**Figure 3A**). Spacing the fluorophore slightly away from the particle surface prevents fluorescence quenching and due to the high local electromagnetic field, results in a large increase in the photoemission from the molecule (**Figure 3B**).

Antimicrobial Applications

The antimicrobial effects of silver can be traced back to the Greeks and Romans, who extended the potability of water by storing it in silver vessels. Silver ions are released from the container walls and provide an antimicrobial effect via a silver ion interaction with thiol groups of vital bacterial enzymes and proteins. This affects cellular respiration and transport of ions across membranes, resulting in cell death.^{4,5} Additional antimicrobial pathways specific to silver nanoparticle toxicity have also been proposed. Silver nanoparticles can anchor and subsequently penetrate the bacterial cell wall, leading to damaging structural changes in the cell membrane.⁶ Generation of reactive oxygen species at the surface of the silver nanoparticles can result in oxidative stress providing a further mechanism for cell damage.⁷ The specific toxicity to bacteria, while maintaining low toxicity for humans, has led to the integration of silver nanoparticles in a wide variety of products including wound dressings, packaging materials, and antifouling surface coatings.

A central mechanism of silver nanoparticle antimicrobial activity is to provide a high surface area source for silver ions. In an aqueous environment, the particles oxidize in the presence of oxygen and protons according to the stoichiometric reaction



releasing Ag^+ ions as the particle surface dissolves. As the concentration of silver ions in solution increases, an equilibrium state is approached and silver dissolution slows. However, if there are molecules that have an affinity for silver in the local environment, such as thiols or chlorine, the concentration of free silver ions in solution remains low, and silver ion dissolution from the silver nanoparticles continues. Silver nanoparticle's long-term antimicrobial effectiveness relies on the maintenance of an efficacious concentration of silver ions in a wide variety of different solutions.

Silver Ion Release Rates

Silver ion release rates from silver nanoparticles depend on a number of factors including nanoparticle size, shape, capping agent, aggregation state, and the environment. The smallest particle sizes typically have the fastest ion release rates due to the high surface energy of highly curved or strained nanoparticle surfaces. Shape also contributes to the ion release rate. **Figure 4** shows the ion release profiles of different-sized spherical nanoparticles and silver nanoplates.

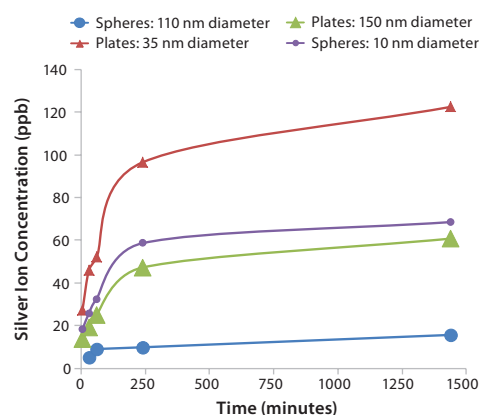


Figure 4. Silver ion release as a function of time, for silver spheres and nanoplates of different sizes. The same mass of silver is used in each sample.

As expected, smaller (10 nm diameter) silver nanospheres exhibit a significantly higher release rate and final ion concentration than larger (110 nm diameter) nanospheres. Anisotropic silver nanoplates have significantly different ion release rates than spherical particles. Large silver nanoplates, with an average diameter of 150 nm, have nearly the same silver concentration profile over time as the 10 nm spherical silver particles, and the 35 nm diameter plates exhibit silver ion concentrations nearly twice as high as the smaller silver spheres.

The functionalization of the surface also plays a role in the ion release rate with tightly bound thiol-containing capping agents generally reducing release rates compared to more easily displaceable stabilizing molecules such as citrate. Aggregation of the particles will also decrease ion release rates but the larger impact of aggregation is the change of kinetics and distribution due to settling. The factor that affects ion release rate the most is the nanoparticle environment. Elevated temperatures, the presence of chlorine, thiols, and oxygen all affect the release rate. In some physiological media, complete dissolution of silver nanoparticles can occur in just a few hours.

By understanding how the physical and chemical properties of silver nanoparticles impact release rates, silver nanomaterial composites can be designed so that a desired ion release profile can be obtained. This optimization is important so that the amount of required silver can be minimized, leading to a more cost-effective product that has minimal long-term environmental impact.

Tagging and Targeting for Bio-imaging

Silver nanoparticles absorb and scatter light with extraordinary efficiency and are utilized in tagging and imaging applications. The high scattering cross-section of the nanoparticles allow for individual silver nanoparticles to be imaged under dark field microscopy (**Figure 5**) or hyperspectral imaging systems.⁸ By coupling biomolecules such as antibodies or peptides to the surface of the silver nanoparticles, the silver nanoparticles can be targeted to specific cells or cellular components. Attachment of targeting molecules to the surface can be done via absorption onto the nanoparticle surface or through either covalent coupling or physisorption. Physisorption is typically performed using silver nanoparticles with an easily displaceable capping agent such as citrate. By adjusting the pH and salt concentration, silver nanoparticle antibody conjugates with high affinity and low non-specific background can be obtained. Improved performance can be achieved by covalently binding the antibody to the surface. One covalent approach is to functionalize the silver nanoparticles with mixed monolayers of thiolated PEG molecules, where a portion of the thiolated PEG contains carboxylic acid functionality and the remainder of the molecules are inert (methoxy-terminated). Using an ethyl(dimethylaminopropyl) carbodiimide (EDC) coupling, the carboxylic acid can then be covalently linked to free amines on the antibody, yielding a targetable silver nanoparticle probe.

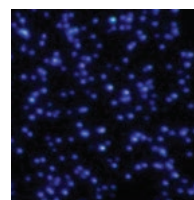


Figure 5. Dark field microscopy image of 60 nm diameter silver nanospheres.

Nanomedicine and Nanosafety

The use of silver nanoparticles in *in vitro* and *in vivo* applications is rapidly increasing. In addition to silver nanoparticle-based ultrabright fluorescent labeling and Surface Enhanced Raman Spectroscopy (SERS) nanotags, other applications for silver nanoparticles include their use as thermal sources for hyperthermia and thermally modulated drug release from particle surface coatings. Silver nanoparticles can also be incorporated into core/shell constructs. An amorphous silica shell grown uniformly onto silver nanoparticle cores can have a variety of functional groups conjugated into the shell, providing a means for electrostatic or other interactions between the shell and a molecule. Fluorophores, drug molecules, or other high molecular weight organic molecules can be integrated within the shell for *in vitro* or *in vivo* labeling or drug delivery applications.

Many of the future biomedical applications of silver nanoparticles will require that the interaction of the nanoparticle with biological systems is well understood. For *in vivo* applications, a major challenge is designing particles that have long circulation times and low toxicity. Experiments to optimize nanoparticle performance in *in vivo* systems are complicated by the complexity of both the nanoparticles themselves and their environment. The biological fate and transport of the nanoparticle is dependent not only on the primary characteristics of the particles (e.g.,

core chemistry, size, shape, crystallinity, surface, and aggregation state), but also on secondary characteristics that rely on the nanoparticle interaction with the target biological systems (e.g., protein corona, dissolution rate, biodistribution).⁹ Experiments performed with sets of precisely manufactured and well-characterized nanomaterials with only a single modified property (e.g., core chemistry, size, shape, or surface) provide insight into the biological response of the varied property and assist in determining the optimal characteristics for effective performance.

Conclusions and Future Outlook

The unique optical properties and broad-based antimicrobial properties of silver nanoparticles have led to a rapid rise in the incorporation of silver nanoparticles in biological applications. The high level of control that is available for controlling size, shape, and surface of silver nanoparticles provides a powerful library for not only generating functional materials

for biological applications but also for understanding the fundamental mechanisms of transport and interaction of nanoparticles in biological systems. This understanding, coupled with the construction of more complex multifunctional silver nanocomposites, will enable the next generation of silver nanoparticle-based probes, devices, and therapeutics.

References

- (1) Moskovits, M., *J. Chem. Phys.*, **1978**, *69*, 4159.
- (2) Kneipp, K., Wang, Y., Kneipp, H., Perelman, L.T., Itzkan, I., *Phys. Rev. Lett.*, **1997**, *78*, 1667.
- (3) Geddes, C.D., Lakowicz, J.R., *J. Fluoresc.*, **2002**, *12*, 121.
- (4) Rai, M., Yadav, A., Gade, A., *Biotech. Adv.*, **2009**, *27*, 76.
- (5) Marambio-Jones, C., Hoek, E. M. V., *J. Nanopart. Res.*, **2010**, *12*, 1531.
- (6) Sonodi, I., Salopek-Sonodi, B., *J. Colloid Interface Sci.*, **2004**, *275*, 177.
- (7) Kim, J.S., Kuk, E., Yu, K., Kim, J.H., Park, S.J., Lee, H.J., Kim, S.H., Park, Y.K., Hwang, C.-Y., Kim, Y.K., Lee, Y.S., Jeong, D.H., Cho, M.H., *Nanomedicine*, **2007**, *3*, 95.
- (8) Carlson, C., Hussain, S.M., Schrand, A.M., Braydich-Stolle, L.K., Hess, K.L., Jones, R.L., Schlager, J.J., *J. Phys. Chem. B*, **2008**, *112*, 13608.
- (9) Powers, K.W., Palazuelos, M., Moudgil, B.M., Roberts, S.M., *Nanotoxicology*, **2007**, *1*, 42.

Silver Nanomaterials

For a complete list of available materials, visit aldrich.com/nanopowders.

Name	Dimensions	Purity & Concentration	Form	Prod. No.
Silver	particle size <150 nm	99% trace metals basis	nanopowder	484059-5G
	particle size <100 nm	99.5% trace metals basis	nanopowder	576832-5G
Silver, dispersion	particle size ~157 nm	0.25 mM in H ₂ O	dispersion nanoparticles	675318-5ML
	particle size 10 nm (TEM)	0.02 mg/mL in aqueous buffer	nanoparticles	730785-25ML
	particle size 20 nm (TEM)	0.02 mg/mL in aqueous buffer	nanoparticles	730793-25ML
	particle size 40 nm (TEM)	0.02 mg/mL in aqueous buffer	nanoparticles	730807-25ML
	particle size 60 nm (TEM)	0.02 mg/mL in aqueous buffer	nanoparticles	730815-25ML
	particle size 100 nm (TEM)	0.02 mg/mL in aqueous buffer	nanoparticles	730777-25ML
	<100 nm (particle size TEM)	5 wt. % in ethylene glycol	nanoparticles	758329-5G 758329-25G
Silver nanowires	diam × L 115 nm × 20–50 μm	0.5% (isopropyl alcohol suspension)	liquid (suspension)	739448-25ML
	diam × L 60 nm × 10 μm	0.5% in isopropanol (suspension)	liquid (suspension)	739421-25ML
	diam × L 120–150 nm × 20–50 μm	0.5% (isopropyl alcohol suspension)	liquid (suspension)	778095-25ML

Silver Salts

For a complete list of available materials, visit aldrich.com/salts.

Name	Formula	Purity	Form	Prod. No.
Silver carbonate	Ag ₂ CO ₃	99%	powder and chunks	179647-5G 179647-25G 179647-100G
		≥99.0%	powder	85150-10G 85150-50G
Silver carbonate on Celite®	Ag ₂ CO ₃	-	powder and chunks	363685-5G 363685-25G
Silver chloride	AgCl	99.999% trace metals basis	powder and chunks	204382-1G 204382-5G 204382-25G
Silver cyanate	AgOCN	99%	powder and chunks	244694-10G 244694-50G
Silver(I) fluoride	AgF	≥99.9% trace metals basis	powder	226858-1G 226858-5G 226858-25G
		99%	powder	226866-5G 226866-25G
Silver nitrate	AgNO ₃	99.9999% trace metals basis	crystalline	204390-1G 204390-10G 204390-50G 204390-250G 204390-2KG

Name	Formula	Purity	Form	Prod. No.
Silver nitrite	AgNO ₂	99.98% trace metals basis	powder	545015-5G 545015-25G
	AgNO ₂	99%	powder	227188-10G 227188-50G
Silver <i>p</i> -toluenesulfonate	CH ₃ C ₆ H ₄ SO ₃ Ag	≥99%	powder	176427-10G 176427-25G

Gold Nanorods

For a complete list of available materials, visit aldrich.com/goldnanomaterials.

Name	Dimensions	Absorption	Concentration	Form	Prod. No.
Gold nanorods	diam. × L 10 × 38 nm	780 nm	> 30 µg/mL	colloidal suspension dispersion in H ₂ O	716812-25ML
	diam. × L 10 × 41 nm	808 nm	> 30 µg/mL	colloidal suspension dispersion in H ₂ O	716820-25ML
	diam. × L 10 × 45 nm	850 nm	> 30 µg/mL	colloidal suspension dispersion in H ₂ O	716839-25ML
	diam. × L 25 × 60 nm	650 nm	> 45 µg/mL	colloidal suspension dispersion in H ₂ O	771686-25ML
	diam. × L 25 × 47 nm	600 nm	> 45 µg/mL	colloidal suspension dispersion in H ₂ O	771651-25ML
	diam. × L 25 mm × 34 nm	550 nm	> 45 µg/mL	colloidal suspension dispersion in H ₂ O	771643-25ML
	diam. × L 10 × 59 nm	980 nm	> 30 µg/mL	colloidal suspension dispersion in H ₂ O	776661-25ML
	diam. × L 10 × 50 nm	900 nm	≥ 30 µg/mL	dispersion in H ₂ O	776653-25ML
	diam. × L 10 × 67 nm	980 nm	> 30 µg/mL	colloidal suspension dispersion in H ₂ O	776688-25ML

Gold Nanoparticles Stabilized in Citrate

For a complete list of available materials, visit aldrich.com/goldnanomaterials.

Name	Dimensions	Absorption	Concentration	Prod. No.
Gold nanoparticles	diameter 5 nm	510-525 nm	~ 5.5E+13 particles/mL	741949-25ML 741949-100ML
	diameter 10 nm	510-525 nm	~ 6.0E+12 particles/mL	741957-25ML 741957-100ML
	diameter 20 nm	518-522 nm	~ 7.2E+11 particles/mL	741965-25ML 741965-100ML
	diameter 30 nm	524-527 nm	~ 1.8E+11 particles/mL	741973-25ML 741973-100ML
	diameter 40 nm	529-533 nm	~ 7.2E+10 particles/mL	741981-25ML 741981-100ML
	diameter 50 nm	535-539 nm	~ 3.5E+10 particles/mL	742007-25ML 742007-100ML
	diameter 60 nm	538-544 nm	~ 1.9E+10 particles/mL	742015-25ML 742015-100ML
	diameter 80 nm	551-557 nm	~ 7.8E+9 particles/mL	742023-25ML 742023-100ML
	diameter 100 nm	564-574 nm	~ 3.8E+9 particles/mL	742031-25ML 742031-100ML
	diameter 200 nm	-	~ 1.9E+9 particles/mL	742066-25ML 742066-100ML
	diameter 250 nm	-	~ 7.1E+8 particles/mL	742074-25ML 742074-100ML
	diameter 300 nm	-	~ 4.5E+8 particles/mL	742082-25ML
	diameter 400 nm	-	~ 1.9E+8 particles/mL	742090-25ML
	diameter 150 nm	-	~ 3.6E+9 particles/mL	742058-25ML 742058-100ML
	diameter 15 nm	510-525 nm	-	777137-25ML 777137-100ML

SEMICONDUCTOR NANOWIRES

Small Materials—Big Impact

Aldrich® Materials Science is proud to announce the enhancement of our metallic nanowire offer with the introduction of oxide nanomaterials with extremely high aspect ratios.

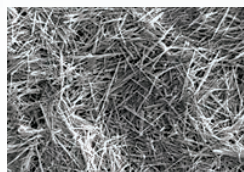
The basic properties of nanomaterials are directly related to their morphology and one-dimensional nanostructures possess significant potential owing to their combination of nanoscale diameters and macroscale lengths.

Nanowire materials have found applications in:

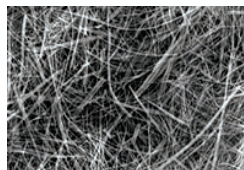
- Photovoltaics
- Piezoelectrics
- Electronics
- Nanocomposites
- Coatings
- Catalyst Supports

Recently introduced semiconductor nanowires include:

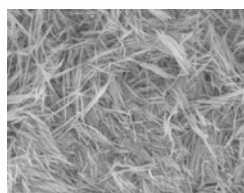
Name	Composition	Dimensions (D × L)	Form	Prod. No.
Zinc Oxide	ZnO	50 nm × 300 nm	Nanowires	773980
Zinc Oxide	ZnO	90 nm × 1 μm	Nanowires	773999
Zinc Oxide	ZnO	300 nm × 4-5 μm	Nanowires	774006
Titanium(IV) Oxide	TiO ₂	~10 nm × ~10 μm	Nanowires	774529
Titanium(IV) Oxide	TiO ₂	~100 nm × ~10 μm	Nanowires	774510
Tungsten(VI) Oxide	WO ₃	~50 nm × ~10 μm	Nanowires	774537
Nickel(II) Oxide	NiO	~20 nm × ~10 μm	Nanowires	774545
Silver	Ag	115 nm × 20-50 μm	Suspension (Isopropanol)	739448
Silver	Ag	60 nm × 10 μm	Suspension (Isopropanol)	739421



Tungsten(VI) Oxide Nanowires
[Product 774537](#)

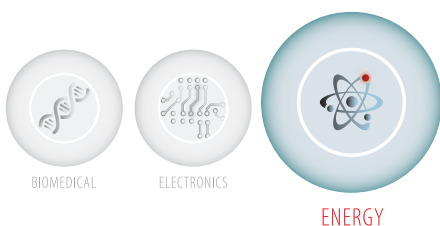


Titanium(IV) Oxide Nanowires
[Product 774510](#)



Zinc Oxide Nanowires
[Product 774006](#)

For a full listing of nanowire products, visit aldrich.com/nanowires



BIOMEDICAL

ELECTRONICS

ENERGY

Aldrich[®] Materials Science Congratulates

DR. LEI JIANG

Recipient of the MRS Mid-Career Researcher Award

The Materials Research Society (MRS) has selected Lei Jiang, co-chairman of editorial advisory boards including *Advanced Functional Materials*, *Advanced Materials Interfaces*, *Soft Matter*, *MPG*, *Asia Materials*, *Biomicrofluidics*, *Nano Research*, *Journal of Organic Biochemistry* and *Materials Research Innovations* as the 2014 MRS Mid-Career Researcher Award winner. Jiang was awarded the MRS Mid-Career research award for his research focusing on bio-inspired interfacial materials with super-wettability.

The MRS Mid-Career Researcher Award, endowed by Aldrich[®] Materials Science, recognizes exceptional achievements in materials research made by mid-career professionals.

About Dr. Jiang

Dr. Lei Jiang obtained his B.S. degree in physics and Ph.D. from Jilin University as a China–Japan joint course. After working as a postdoctoral fellow at Tokyo University, he became a senior researcher at the Kanagawa Academy of Sciences and Technology. Jiang then joined the Institute of Chemistry, Chinese Academy of Sciences (CAS) where he presently serves as professor and also set up the School of Chemistry and Environmental Engineering at Beihang University. He has published more than 400 papers in journals ranging from *Science* to the *Journal of the American Chemical Society*. He has also won numerous awards, including academian of the CAS in 2009, Fellow of the Royal Society of Chemistry, the TWAS Chemistry Award in 2011, and the Heliang-Heli Prize in 2013.

